

AD-A096 379

NAVAL POSTGRADUATE SCHOOL MONTEREY CA

F/G 19/1

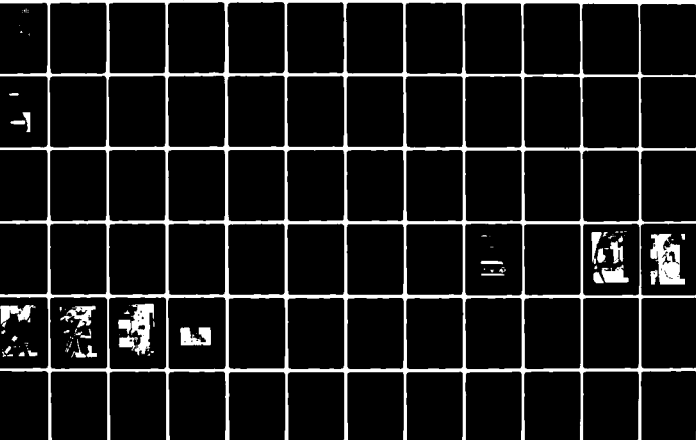
BALL MOTION IN A BALL-OBTURATED TUBULAR PROJECTILE.(U)

JAN 81 R H MUNN, J W BLOOMER

UNCLASSIFIED NPS69-81-001

NL

1 of 1  
AD-A096 379



END  
DATE  
FILMED  
4-81  
DTIC

AD A 096379

LEVEL II

2

NPS69-81-001

NAVAL POSTGRADUATE SCHOOL  
Monterey, California



DTIC  
ELECTE  
MAR 16 1981  
S E D

BALL MOTION IN A BALL-OBTURATED  
TUBULAR PROJECTILE

R. H. Nunn  
J. W. Bloomer II

January, 1981

Final report for period ending 31 December, 1980

Approved for public release; distribution unlimited

Prepared for:  
Technology Programs Management Office (Code 3205)  
Naval Weapons Center, China Lake, CA 93555

81 3 16 096

DBG FILE COPY

NAVAL POSTGRADUATE SCHOOL  
Monterey, California

J. J. Ekelund, RADM, USN  
Superintendent


D. A. Schrady  
Acting Provost

This report documents progress for the period ending 31 December, 1980, in the project titled "Ball-Obtured Spinning Tubular Projectile."


The work reported herein has been monitored and supported by the Technology Programs Management Office (Code 3205), Naval Weapons Center China Lake, California, and was initiated by Work Request No. N60530-WR30134.

Reproduction of all or part of this report is authorized.

This report was prepared by:

  
ROBERT H. NUNN  
Associate Professor  
Department of Mechanical Engineering

Reviewed by:

  
P. J. Marito, Chairman  
Department of Mechanical  
Engineering

Released by:

  
William M. Tolles  
Dean of Research

UNCLASSIFIED

SECURITY CLASSIFICATION OF THIS PAGE (When Data Entered)

14 REPORT DOCUMENTATION PAGE		READ INSTRUCTIONS BEFORE COMPLETING FORM
1. REPORT NUMBER NPS69-81-001 ✓	2. GOVT ACCESSION NO. AD-A096379	3. RECIPIENT'S CATALOG NUMBER 9
4. TITLE (and Subtitle) 6 BALL MOTION IN A BALL-OBTURATED TUBULAR PROJECTILE	5. TYPE OF REPORT & PERIOD COVERED Final report, for period ending 31 December, 1980	
7. AUTHOR(s) 10 R. H./Nunn J. W./Bloomer, II	8. CONTRACT OR GRANT NUMBER(s)	
9. PERFORMING ORGANIZATION NAME AND ADDRESS Naval Postgraduate School Monterey, California 93940	10. PROGRAM ELEMENT, PROJECT, TASK AREA & WORK UNIT NUMBERS 11	
11. CONTROLLING OFFICE NAME AND ADDRESS Technology Programs Management Office (Code 3205) Naval Weapons Center China Lake, CA 93555	12. REPORT DATE January 1981	
14. MONITORING AGENCY NAME & ADDRESS (if different from Controlling Office)	13. NUMBER OF PAGES 84	
	15. SECURITY CLASS. (of this report) UNCLASSIFIED	
15a. DECLASSIFICATION/DOWNGRADING SCHEDULE		
16. DISTRIBUTION STATEMENT (of this report) Approved for public release; distribution unlimited.		
17. DISTRIBUTION STATEMENT (of the abstract entered in Block 20, if different from Report)		
18. SUPPLEMENTARY NOTES		
19. KEY WORDS (Continue on reverse side if necessary and identify by block number) Gyro, Gyrodynamics, Tubular projectile, Obturator		
20. ABSTRACT (Continue on reverse side if necessary and identify by block number) When a ball with a concentric hole through it is suspended within a spinning tubular projectile the ball will rotate in such a way that its hole is aligned with the axis of spin of the projectile. The ball thus serves as an automatic obturator--plugging the projectile while the two bodies are within the gun barrel and rotating to open the tubular passage following exit from the muzzle. The motion of the ball is gyrodynamic in nature and highly dependent upon the external moments on the ball that arise because of its motion		

DD FORM 1473

EDITION OF 1 NOV 63 IS OBSOLETE  
S/N 0102-014-66011

111

UNCLASSIFIED

SECURITY CLASSIFICATION OF THIS PAGE (When Data Entered)

251450 Jm

UNCLASSIFIED

SECURITY CLASSIFICATION OF THIS PAGE/When Data Entered

relative to the spinning projectile.

This report presents the results of an analytical and experimental study to provide an understanding of such motions in as complete a sense as is possible. The general equations of motion are formulated together with appropriate mathematical expressions for the external moments. These moments have their origins in the forces acting on the ball (gravity and aerodynamic forces are considered) which, in the presence of relative motion between the ball and the projectile, lead to sliding friction torques. Torques due to fluid shear are also considered but these are found to be relatively insignificant.

Exact solutions are obtained using standard numerical techniques. In addition, a linear form is developed and these solutions lead to useful approximations that are valid over a broad range of operating conditions.

Experiments are described in which the general validity of the theoretical models (exact and linear) is demonstrated for cases in which there is little or no aerodynamic load. The experiments, together with the linear approximation, lead to a semi-empirical method for determining the effective coefficient of sliding friction for such systems.

A model is proposed to account for aerodynamic loading and sensitivity studies are conducted to determine the nature and scope of the influence of various design parameters upon system performance. The linear approximation is proposed as a useful design guide when applied with due awareness of its limitations. In addition, a design criterion is presented by means of which it is possible to avoid designs that lead to operation in a "hovering" region. Such operation leads to prolonged delays in ball opening time. Application of the design criterion leads to ball/projectile designs that are optimum from the point of view of minimum ball opening time.

Accession For	
NTIS GRA&I	<input checked="checked" type="checkbox"/>
DTIC TAB	<input type="checkbox"/>
Unannounced	<input type="checkbox"/>
Justification	
By	
Distribution/	
Availability Codes	
Avail and/or	
Dist	Special
A	

## SUMMARY

✓ When a ball with a concentric hole through it is suspended within a spinning spherical cavity the ball will rotate in such a way that its hole is aligned with the axis of spin of the cavity. If it is mounted within a spinning tubular projectile, the ball can serve as an automatic obturator--plugging the projectile while the two bodies are within the gun barrel and rotating to open the tubular passage following exit from the muzzle. The motion of the ball is gyrodynamic in nature and highly dependent upon the external moments on the ball that arise because of its motion relative to the spinning cavity.

This report presents the results of an analytical and experimental study to provide an understanding of such motions in as complete a sense as is possible. The general equations of motion are formulated together with appropriate mathematical expressions for the external moments. These moments have their origins in the forces acting on the ball (gravity and aerodynamic forces are considered) which, in the presence of relative motion between the ball and the projectile, lead to sliding friction torques. Torques due to fluid shear are also considered but these are found to be relatively insignificant.

Exact solutions are obtained using standard numerical techniques. In addition, a linear form is developed and these solutions lead to useful approximations that are valid over a broad range of operating conditions. ✎

Experiments are described in which the general validity of the theoretical models (exact and approximate) is demonstrated for cases in which there is little or no aerodynamic load. The experiments, together

with the linear approximation, lead to a semi-empirical method for determining the effective coefficient of sliding friction for such systems.

A model is proposed to account for aerodynamic loading and sensitivity studies are conducted to determine the nature and scope of the influence of various design parameters upon system performance. The linear approximation is proposed as a useful design guide when applied with due awareness of its limitations. In addition, a design criterion is presented by means of which it is possible to avoid designs that lead to operation in a "hovering" region. Such operation leads to prolonged delays in ball opening time. Application of the design criterion leads to a ball/projectile design that is optimum with respect to ball opening time.

## TABLE OF CONTENTS

<u>SUMMARY</u> .....	v
<u>INTRODUCTION</u> .....	1
RECENT DEVELOPMENTAL STUDIES .....	2
<u>Range Tests</u> .....	2
<u>Target Impact Tests</u> .....	3
<u>Weapons System Compatibility</u> .....	4
<u>Internal Shock Wave Considerations</u> .....	4
PURPOSE OF STUDY .....	5
<u>ANALYSIS</u> .....	10
DEVELOPMENT OF THE EQUATIONS OF MOTION .....	10
EXPRESSION OF THE EXTERNAL MOMENTS .....	15
<u>Torque Due to Fluid Shear</u> .....	15
<u>Torque Due to Sliding Friction</u> .....	16
<u>Gravity load.</u> .....	18
<u>Axial aerodynamic load.</u> .....	19
<u>Consideration of the Relative Angular Velocity Vector</u> .....	21
EXACT SOLUTIONS FOR TYPICAL SYSTEM PARAMETERS .....	24
<u>Consideration of Projectile Angular Velocity</u> .....	25
<u>Gravity Load</u> .....	25
<u>Axial Aerodynamic Load</u> .....	29
<u>LINEAR APPROXIMATIONS</u> .....	33
RESULTS COMPUTED FROM THE LINEAR APPROXIMATIONS .....	38
<u>EXPERIMENTATION</u> .....	41
EXPERIMENTAL APPARATUS .....	41
EXPERIMENTAL PROCEDURE .....	48



TABLE OF CONTENTS (continued)

EXPERIMENTAL DETERMINATION OF THE COEFFICIENT OF SLIDING FRICTION -----	53
DISCUSSION OF THE EXPERIMENTAL RESULTS -----	53
<u>SENSITIVITY TESTS AND DESIGN GUIDES FOR AERODYNAMIC LOADING</u> -	56
SENSITIVITY ANALYSIS -----	58
<u>Geometry effects.</u> -----	59
<u>Material effects.</u> -----	61
<u>Coefficient of sliding friction.</u> -----	61
<u>Launch conditions.</u> -----	65
DESIGN GUIDES -----	65
<u>CONCLUSIONS</u> -----	70
<u>LIST OF REFERENCES</u> -----	72
<u>LIST OF SYMBOLS</u> -----	74
<u>DISTRIBUTION</u> -----	76

## INTRODUCTION

### BACKGROUND

As early as 1858, the potential benefits of tubular projectiles were recognized for specific purposes. In that year, Joseph Whitworth (Whitworth Threads) wrote about and included an illustration of the tubular projectile in the section on Rifled Firearms of his Miscellaneous Papers on Mechanical Subjects [1]<sup>1</sup>. The projectile devised by Whitworth was hexagonal, with a circular hole, and he noted its particular "...effectiveness in perforating elastic materials which prevented them from closing up." Whitworth further observed that the tubular projectile, which utilized a wooden sabot, penetrated deeper into masonry than any with which he was acquainted.

According to Charters and Thomas [2], the "Krnka-Hebler" projectile was reported in the Allgemeine Schweizerische Militarzeitung as having been so successful that the Ordnance Department in the United States carried out firing tests of caliber .30 tubular projectiles in 1894. A description of those test firings and an updating of the results, performed by I.E. Segal, is included in Ref. 2. In the 1894 tests, a vulcanized fiber sabot was used to seal the projectile while in the barrel.

The purpose of the 1894 test was to compare trajectories of standard and tubular projectiles. This was done by comparing the vertical drop on target at a given range. Segal's report indicates that the drag coefficients computed from the 1894 results agree closely with those of Charters and Thomas [2], even though the latter work was reported fifty years later (1944) and utilized more sophisticated experimental apparatus.

---

<sup>1</sup>Numbers appearing in brackets refer to the list of references.

## RECENT DEVELOPMENTAL STUDIES

The result obtained by independent researchers as to the relative merits of the tubular projectile as an alternative to the conventional round are contradictory. It seems as if there was as much research devoted to discrediting the tubular projectile as there was to investigating its merits. Frank and McLaughlin [3] have accumulated a great deal of data from various sources in an attempt to "objectively compare" the merits of the tubular and "conventional shapes". The authors concluded that the tubular has no particular advantages over "well designed" conventional projectile shapes. Their findings disagree with many of those discussed in the following sections.

### Range Tests

Winchenbach, Daniel and Edgar [4] conducted range tests of six configurations of tubular projectiles and concluded that the drag coefficients were significantly lower than the standard High Explosive Incendiary (HEI) projectile of the same caliber. Only projectiles of the same bore size were compared. The experimental models were constructed from standard 20-mm ammunition by boring various hole sizes to obtain "...area ratios ( $A_t/A_i$ ) of 0.7, 0.8, 0.9, and 1.0." Where  $A_t$  is the throat area and  $A_i$  is the inlet area of the projectile. The drag coefficients of the projectiles with area ratios of 0.8, 0.9, and 1.0 were less than half that of the projectile with area ratio of 0.7. The higher drag coefficient was attributed to the underexpanded flow at the exit resulting in high base drag.

Range tests conducted for the concept evaluation of the 20-mm tubular projectile for the Vulcan Weapons System [5] showed that the tubular projectile performed better than the standard HEI round, with lower drag, shorter time of flight for a given range (30 percent shorter at 1000 meters, 40 percent shorter at 2000 meters) and similar dispersion characteristics on target.

Recent tests at the Naval Weapons Center, China Lake, California of the Ball-Obtured Tubular Projectile (BOT) have shown a definite advantage in that the low

drag of the tubular projectile means slower retardation of velocity and hence a higher terminal kinetic energy [6]. (The BOT is the object of this investigation and will be described in detail in later sections of this report.)

#### Target Impact Tests

The higher the energy delivered to the target, the greater the damage. Since kinetic energy is directly proportional to the first power of mass and to the square of the velocity, if a tubular projectile has relatively less mass this maybe compensated by a higher muzzle velocity. However, a reduction in mass to obtain higher muzzle velocities may not be necessary, depending upon the imposed performance criteria.

Target impact studies have been carried out with various projectile configurations and target types. Rhethorst, et.al. [7] conducted impact studies of 7.62-mm tubular projectiles on helmets. Tests showed that even with the same energy of impact, the tubular projectile penetrated further.

Kitchen and Keeser [8] conducted studies for the Air Force on the impact effectiveness of tubular projectiles on simulated aircraft fuel cells. These tests were conducted with steel and depleted uranium (DU) tubular projectiles and standard 20-mm HEI projectiles. The projectiles were fired at double panels at varying degrees of obliquity. Of the forty-seven tests of the steel tubular projectiles which impacted the target, twenty breached the rear panel when fired at angles up to 70°. The DU projectiles breached the rear panel even at angles of 85° and fires were started in three of the five DU tests. The standard M56 HEI projectiles failed to breach the rear panel in each of five firings even though severe damage to the front panel and two fires occurred.

Brunsvold and Kalivretenos [9] conducted a program to test the effectiveness of the tubular projectile against a simulated cruise missile warhead. Tests were conducted with 20 and 40-mm rounds. Results of those tests are classified, and therefore not presented here. It was noted [9] that due to the

improved stability characteristics of the tubular projectile, only about half the spin rate need be imparted by the rifling in the barrel to obtain the same stability as a standard projectile, with obvious implications with respect to wear.

#### Weapons System Compatibility

For the tubular projectile to be practical, it must be able to interface with existing weapons systems. Reference 5 is a report of the 1978 tests conducted by the Army to evaluate the tubular projectile in the Vulcan weapons system.

Because the nose of the tubular projectile is flat compared to the standard projectile (See Fig. 1), it "...did not lend itself to chambering in the weapon." Personnel safety required that the weapon be remotely operated and therefore only the surface-to-surface performance comparison was made.

The dispersion on target improved for the tubular projectile at ranges of from 700 to 2000 meters. The dispersion varied on the average by only 0.2 mil over the entire range spectrum between the tubular and conventional HEI projectile. However, at 2000 meters, the tubular was better by 0.4 mil. The tubular projectile had a 30 percent shorter flight time at 1000 meters and a 40 percent shorter flight time at 2000 meters than the conventional HEI projectile.

Results of firing of 25-mm and 30-mm tubular projectiles from the Oerlikin KBA and GAU-8/A respectively were reported in part in Ref. 3. Figures comparing Line-of-Sight Penetration Capability vs. Range for a conventional spinner configuration based on the AR-2 shape, a finner configuration based on the F10 shape, and a tubular projectile were shown. The tubular projectile was shown to be inferior in both instances. The report does not indicate the degree of compatibility the tubular configuration has with the guns used.

#### Internal Shock Wave Considerations

From photographs of tubular projectiles in flight [4] and during wind

tunnel testing [7], various shock patterns have been observed at the inlet region and in the wake. The photographs of Figs. 2a-c show the BOT and the conventional projectiles in flight. The sabots used in Refs. 4 and 7 were of the pusher type consisting of a simple base plug. The detached bow shock seen in the photograph of the standard projectile (Fig. 2a) is similar to that of the tubular projectile shown in Fig. 2b with the tubular passage closed (and in Ref. 4 with the sabot attached). With no blockage of the internal passage (Fig. 2c) there was no detached bow shock, with only attached oblique shocks emanating from the lip of the projectile. This latter case allows the possibility of four other internal flow/shock configurations.

- (1) A normal shock standing at the entrance to the projectile;
- (2) A normal shock standing at some intermediate position in the channel;
- (3) A system of oblique shocks present in the channel;
- (4) The channel is devoid of shocks and the flow is shock-free through the channel.

Reference 10 contains a discussion of the shock patterns and the various conditions leading to their existence.

#### PURPOSE OF STUDY

The results of tests and experiments previously mentioned show, for the most part, definite advantages accruing to the tubular projectile over the conventional projectile primarily in the area of lower drag (approximately  $1/2$  to  $1/3$  of conventional [8]) which allows a flatter trajectory and shorter time of flight for a given range [5]. With reference to air combat and anti-missile defense both from a Surface-to-Air and Air-to-Air standpoint, these features are definitely worth further study.

The problem seen from the air platform is that of the discarding sabot or pusher. The solid [4, 5, 7,] or split [8] disk is effective and reliable,

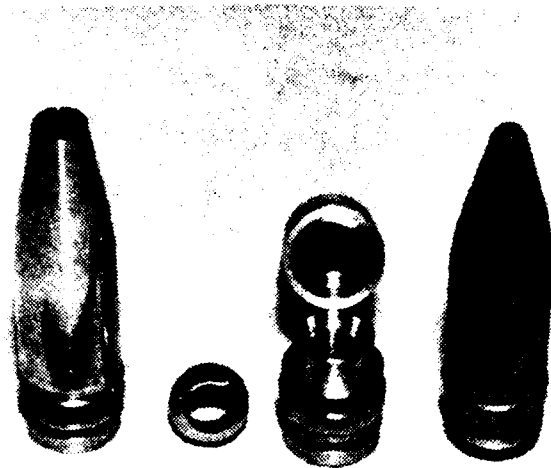


Figure 1. 20-mm Ball Obturated Tubular Projectile (BOT), components, and conventional 20-mm projectile. (Photograph courtesy of NWC, China Lake).

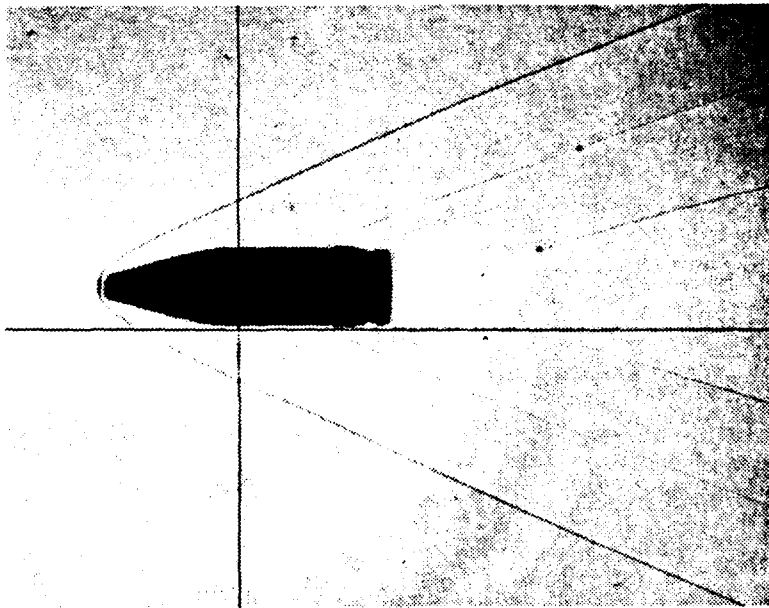


Figure 2a. Standard 20-mm projectile in flight with detached bow shock. (Photograph courtesy of NWC, China Lake).

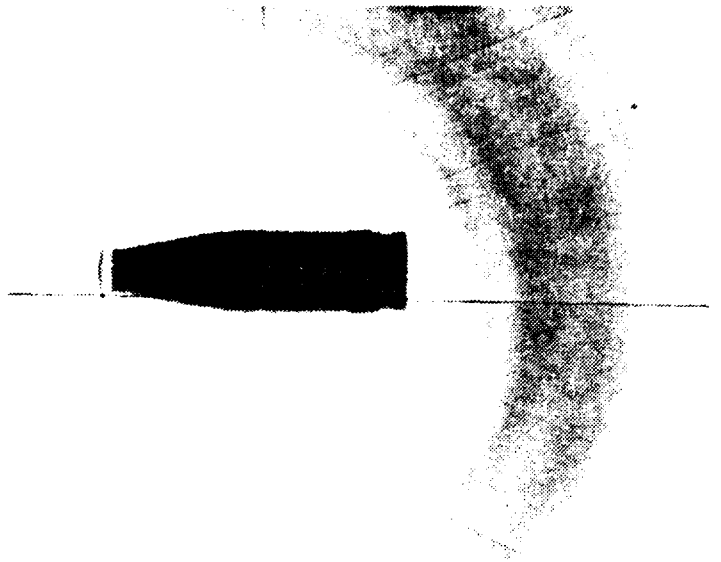


Figure 2b. BOT with passage blocked resulting in detached bow shock. (Photograph courtesy of NWC, China Lake).

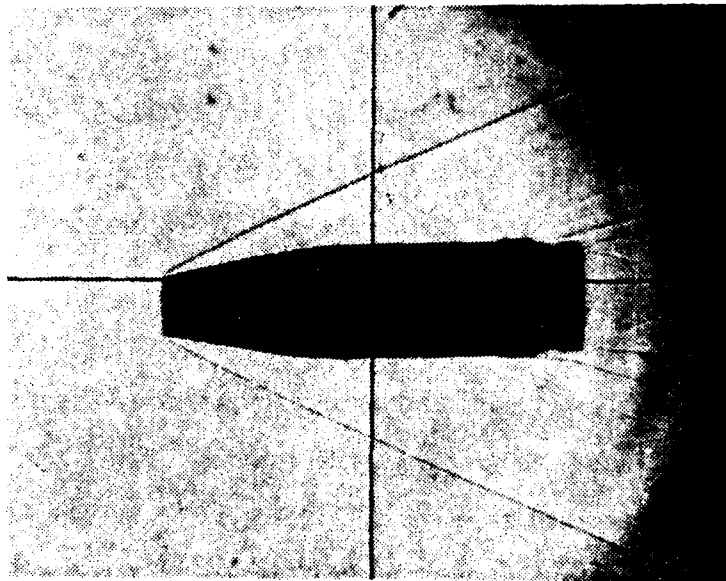


Figure 2c. BOT with no blockage in passage; only attached oblique shocks emanating from the lip of the projectile. (Photograph courtesy of NWC, China Lake).



however, the possibility of ingestion in the aircraft engines prohibits their use. Rhethorst et al., in Ref. 7 illustrates a number of sabot/ obturator designs for use with the tubular projectile, but these are also of the discarding type. They also investigated the possibility of using a consumable sabot [11] which would be burned up as the projectile was transiting the barrel and would be completely consumed as it exited the barrel.

The most recent development has been the BOT which was designed at NWC China Lake, California [6]. The ball obturator has been bored with a hole the same diameter as the hole through the projectile. When loaded, the ball is supported inside the projectile such that the axis through the hole in the ball makes an angle of approximately  $90^\circ$  with the axis of the hole through the projectile (see Fig. 3). Gas pressure from the burning propellant holds the ball obturator fixed with respect to the projectile (as well as to the ball). Upon exiting the barrel, the propellant gas pressure is released and, in its place, forces due to aerodynamic effects come into play. At that time a complex force distribution acts on the ball to cause it to change orientation inside the projectile in such a way as to align the holes. Inertial forces then dominate to maintain this alignment so that the projectile remains fully tubular. There are no separating parts and the opening process is automatic.

The purpose of the study reported herein has been to analytically predict the motion of the ball obturator as a function of time. In support of this purpose, an experimental apparatus was designed and built to simulate the motion of the obturator in order to provide physical evidence of the accuracy of the model and to gain insights into the nature of the motion.

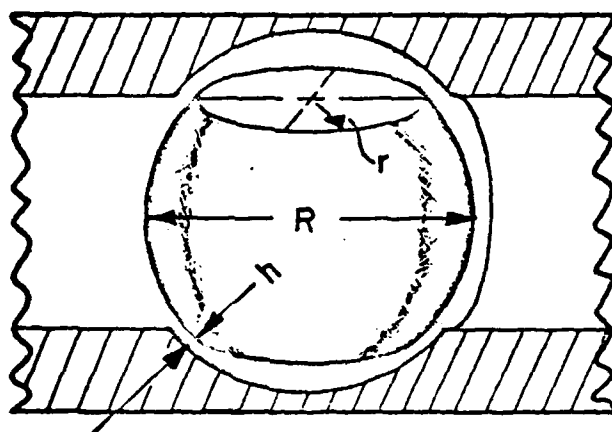


Figure 3. Sketch showing dimensions and positioning of the ball obturator within the spherical cavity.

## ANALYSIS

### DEVELOPMENT OF THE EQUATIONS OF MOTION

The ball obturator is a rigid body of revolution with a system of coordinate axes fixed to the ball (body-fixed axes) having its origin at the mass center of the ball (Fig. 4). These axes are designated x, y, and z, where z is the axis through the hole in the ball.

To describe the motion of the ball relative to the projectile an inertial frame of reference is defined with axes designated X, Y and Z with its origin also at the mass center of the ball. For this analysis it is assumed that the projectile is constrained to rotate about the Z-axis. Because the motion of the ball with respect to the projectile is of special interest it should be noted that components of the ball angular velocity with respect to the X and Y axes are also relative to the projectile, whereas the component with respect to the Z-axis must account for the projectile spin.

The motion may be described by Euler's Modified Equations of Motion for a rigid body of revolution about a fixed point. These are given in Thomson [12] as:

$$A\dot{\omega}_1 + (C-A)\omega_2\omega_3 = M_1 \quad (1a)$$

$$A\dot{\omega}_2 + (A-C)\omega_1\omega_3 = M_2 \quad (1b)$$

$$C\dot{\omega}_3 = M_3 \quad (1c)$$

where

- A = Mass moments of inertia about principal axes perpendicular to the z-axis.
- C = Mass moment of inertia about the principal axis through the hole (z-axis).

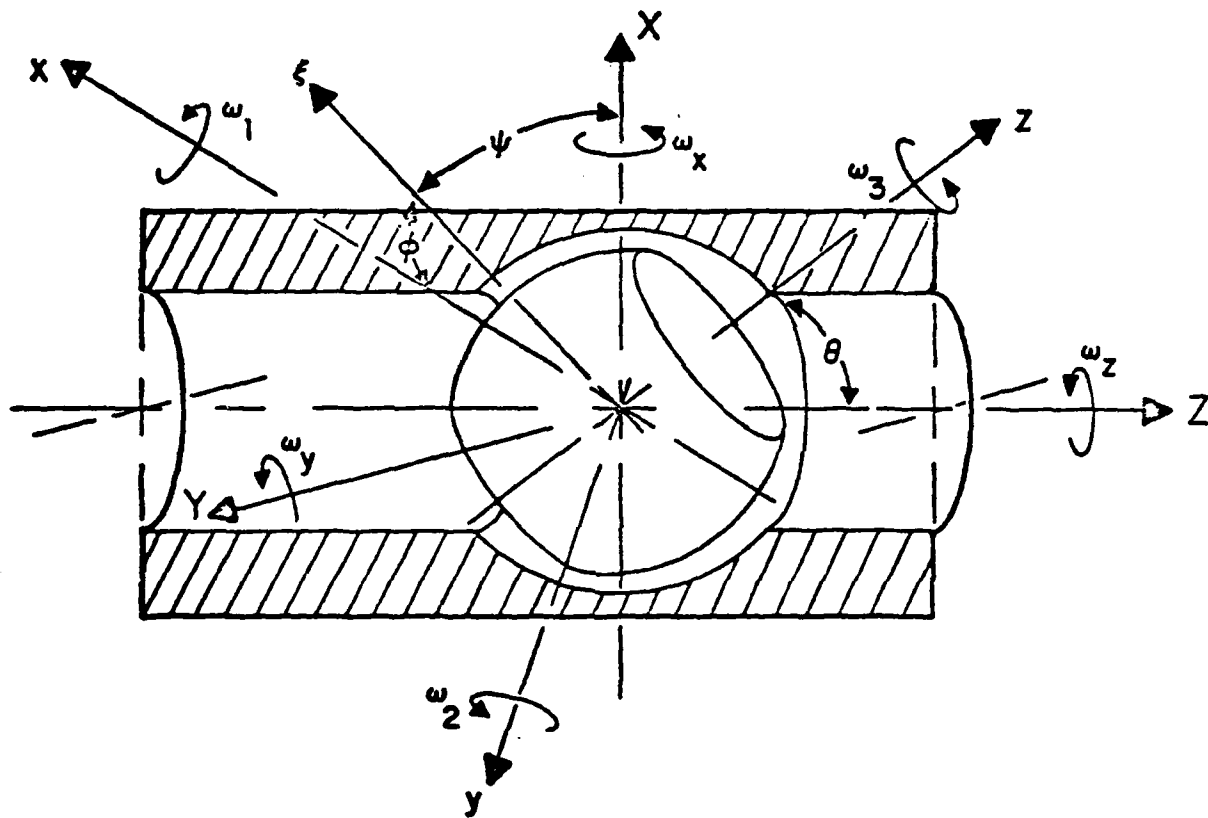


Figure 4. Illustration of coordinate systems and symbols used in the analysis.

$\dot{\omega}_1, \dot{\omega}_2, \dot{\omega}_3$  = Angular accelerations about the body-fixed axes  
x, y, z respectively.

$\omega_1, \omega_2, \omega_3$  = Angular velocities about the body-fixed axes.

$M_1, M_2, M_3$  = External moments acting about the body-fixed  
axes.

The mass moments of inertia for the particular case at hand  
(sphere of radius R with concentric hole of radius r) are given by:

$$A = \frac{4\pi\rho R^5}{15} \left[ \frac{1}{2}(1-\hat{r}^2)^{3/2} (3\hat{r}^2 + 2) + (1 - \hat{r}^2)^{5/2} \right] \quad (2)$$

$$C = \frac{4\pi\rho R^5}{15} (1-\hat{r}^2)^{3/2} (3\hat{r}^2 + 2) \quad (3)$$

where  $\hat{r} = r/R$ .

The symbol  $\lambda$  is introduced here to denote the relative difference  
between the two moments of inertia. That is:

$$\lambda = \frac{C-A}{A}$$

From Eqs. (2) and (3) it is seen that

$$\lambda = \frac{5\hat{r}^2}{\hat{r}^2+4} \quad (4)$$

and since  $0 \leq \hat{r} \leq 1$ ,  $\lambda$  lies in the range  $0 \leq \lambda \leq 1$ .

With  $\lambda$  so defined, Eqs. (1) may be rewritten:

$$\dot{\omega}_1 + \lambda \omega_2 \omega_3 = M_1/A \quad (1a)$$

$$\dot{\omega}_2 - \lambda \omega_1 \omega_3 = M_2/A \quad (1b)$$

$$\dot{\omega}_3 = M_3/C \quad (1c)$$

The orientation of the ball at any time may be described by  
three angles;  $\theta$ ,  $\phi$  and  $\psi$ . These are known as Euler angles and their  
relationships to the coordinate axes already described may be seen in  
Fig. 4. The components of angular velocity  $\omega_1$ ,  $\omega_2$  and  $\omega_3$  in terms of  
the Euler angles are given as [12]:

$$\omega_1 = \dot{\psi} \sin \theta \sin \phi + \dot{\theta} \cos \phi \quad (5a)$$

$$\omega_2 = \dot{\psi} \sin \theta \cos \phi - \dot{\theta} \sin \phi \quad (5b)$$

$$\omega_3 = \dot{\phi} + \dot{\psi} \cos \theta \quad (5c)$$

By differentiating Eqs. (5) with respect to time, the angular accelerations,  $\dot{\omega}_1$ ,  $\dot{\omega}_2$ , and  $\dot{\omega}_3$  may be obtained as

$$\begin{aligned} \dot{\omega}_1 = & \ddot{\psi} \sin \theta \sin \phi + \dot{\psi} (\dot{\theta} \cos \theta \sin \phi + \dot{\phi} \sin \theta \cos \phi) + \ddot{\theta} \cos \phi \\ & - \dot{\theta} \dot{\phi} \sin \phi \end{aligned} \quad (6a)$$

$$\begin{aligned} \dot{\omega}_2 = & \ddot{\psi} \sin \theta \cos \phi + \dot{\psi} (\dot{\theta} \cos \theta \cos \phi - \dot{\phi} \sin \theta \sin \phi) - \ddot{\theta} \sin \phi \\ & - \dot{\theta} \dot{\phi} \cos \phi \end{aligned} \quad (6b)$$

$$\dot{\omega}_3 = \ddot{\phi} + \ddot{\psi} \cos \theta - \dot{\psi} \dot{\theta} \sin \theta \quad (6c)$$

Combination of Eqs. (1), (5), and (6) yields the Euler equations in terms of the Euler angles:

$$\ddot{\psi} \sin \theta \sin \phi + \dot{\psi} (\dot{\theta} \cos \theta \sin \phi + \dot{\phi} \sin \theta \cos \phi) + \ddot{\theta} \cos \phi - \dot{\theta} \dot{\phi} \sin \phi + \lambda (\dot{\psi} \sin \theta \cos \phi - \dot{\theta} \sin \phi) (\dot{\psi} \cos \theta + \dot{\phi}) = M_1 / A \quad (7a)$$

$$\ddot{\psi} \sin \theta \cos \phi + \dot{\psi} (\dot{\theta} \cos \theta \cos \phi - \dot{\phi} \sin \theta \sin \phi) - \ddot{\theta} \sin \phi - \dot{\theta} \dot{\phi} \cos \phi - \lambda (\dot{\psi} \sin \theta \sin \phi + \dot{\theta} \cos \phi) (\dot{\psi} \cos \theta + \dot{\phi}) = M_2 / A \quad (7b)$$

$$\ddot{\psi} \cos \theta - \dot{\psi} \dot{\theta} \sin \theta + \ddot{\phi} = M_3 / C \quad (7c)$$

If Eq. (7a) is multiplied by  $\sin \phi$  and Eq. (7b) by  $\cos \phi$ , and the results are then added, we obtain<sup>1</sup>

$$\ddot{\psi} \sin \theta = (M_1 / A) \sin \phi + (M_2 / A) \cos \phi + \ddot{\theta} [(\lambda + 1) \dot{\phi} + (\lambda - 1) \dot{\psi} \cos \theta]$$

<sup>1</sup>The overbar notation is introduced here to denote dimensional time-dependent quantities. These will subsequently be non-dimensionalized through the use of the initial projectile spin rate.

Similarly, if the multiplication is reversed and the results are subtracted, we have

$$\ddot{\theta} = (\bar{M}_1/A)\cos\phi - (\bar{M}_2/A)\sin\phi - \ddot{\psi}\sin\theta [(\lambda + 1)\dot{\phi} + \lambda\dot{\psi}\cos\theta]$$

Simply rewriting Eq. (7c) we have

$$\ddot{\phi} = \bar{M}_3/C + \ddot{\psi}\dot{\theta}\sin\theta - \ddot{\psi}\cos\theta$$

These are the basic governing equations for the motion of the ball in terms of the Euler angles. They are second order ordinary differential equations, nonlinear, and strongly coupled. Before proceeding further, we shall introduce the convenience of non-dimensionalization of the time-dependent variable. This is accomplished through the use of  $\omega_{p0}$ , the initial rate of spin of the projectile. The equations of motion are unchanged in form except for the terms involving the external moments.

Thus, with the definitions

$$M_1 = \bar{M}_1/A\omega_{p0}^2, M_2 = \bar{M}_2/A\omega_{p0}^2, M_3 = \bar{M}_3/C\omega_{p0}^2$$

we have

$$\ddot{\psi}\sin\theta = M_1\sin\phi + M_2\cos\phi + \dot{\theta} [(\lambda + 1)\dot{\phi} + (\lambda-1)\dot{\psi}\cos\theta] \quad (8)$$

$$\ddot{\theta} = M_1\cos\phi - M_2\sin\phi - \dot{\psi}\sin\theta [(\lambda + 1)\dot{\phi} + \lambda\dot{\psi}\cos\theta] \quad (9)$$

$$\ddot{\phi} = M_3 + \dot{\psi}\dot{\theta}\sin\theta - \ddot{\psi}\cos\theta \quad (10)$$

where  $\dot{\psi} = \bar{\dot{\psi}}/\omega_{p0}$ ,  $\ddot{\psi} = \bar{\ddot{\psi}}/\omega_{p0}^2$ , etc.

The integration of Eqs. (8) - (10) proceeds from a condition in which the ball is fixed to the projectile and spinning with it. The initial values of the precession angle  $\psi$  and the spin angle  $\phi$

are arbitrary and are set to zero for convenience. The appropriate initial conditions are, therefore:

$$\begin{aligned}\theta(0) &= \theta_0 & \dot{\theta}(0) &= 0 \\ \phi(0) &= 0 & \dot{\phi}(0) &= 0 \\ \psi(0) &= 0 & \dot{\psi}(0) &= 1\end{aligned}\tag{11}$$

The central problem yet to be addressed is that of the specification of the external moments  $\bar{M}_1$ ,  $\bar{M}_2$ , and  $\bar{M}_3$  or, in non-dimensional form,  $M_1$ ,  $M_2$ , and  $M_3$ .

#### EXPRESSION OF THE EXTERNAL MOMENTS

The interaction of the ball with the cavity in the spinning projectile is dominated by torques arising from the relative motion between the two bodies. These torques will be opposite to the direction of the relative velocity so that we may begin by specifying that:

$$\underline{M} = -\underline{l}_r M\tag{12}$$

where  $\underline{l}_r = \underline{\omega}_r / |\omega_r|$  = unit vector in the direction of the relative angular velocity

We have considered torques due to both fluid shear and sliding friction.

#### Torque Due to Fluid Shear, $M_f$

Nakabayashi [13] has recently reported the results of a series of experiments to determine the fluid shear acting in the gap between two concentric rotating spheres. Although the details of the flow are



extremely complex [14], the results of Nakabayashi show that the data are well correlated by:

$$C_m = 8\pi(1 + \epsilon)/(3\epsilon Re) \quad \text{for laminar flow} \quad (13)$$

and  $C_m = 0.053[1 + (7/4)\epsilon]/\{\epsilon[1 - (3/2)\epsilon]Re^{0.25}\}$  for turbulent flow, where  $C_m = \bar{M}_f/(\rho R^5 \bar{\omega}_r^2)$ ,  $\epsilon = (h/R) \ll 1$ , and the Reynolds number is given as:

$$Re = R^2 \bar{\omega}_r / \nu.$$

From [13] it is also possible to estimate a transition Reynolds number:

$$Re_t \doteq 70\epsilon^{-1.6}$$

In our experiments (both real and numerical) we have found that relative angular velocities in the range of interest are well below those necessary to stimulate turbulent flow in air so that Eq. (13) is adequate for our purposes. When Eq. (13) is cast in a suitable form we have:

$$\bar{M}_f = 8\pi(1 + \epsilon)\mu R^3 \bar{\omega}_r / (3\epsilon) \quad (14)$$

#### Torque Due to Sliding Friction, $M_s$

In the case of sliding friction the magnitude of the applied torque may be written

$$\bar{M}_s = \mu_s F_n r_m \quad (15)$$

where  $F_n$  is the normal component of the resultant of all forces acting upon the ball and  $r_m$  is the moment arm extending from the point of contact and directed normal to the vector of relative angular velocity.

Since the point of contact must be on the surface of the ball, the position vector of this point,  $\vec{P}$ , must have a magnitude of the ball radius  $R$ . Figure 5 illustrates the geometry for cases to be discussed in which multiple points of contact are distributed along a line. If  $\gamma$  and  $\beta$  are the location angles of a point of contact, as illustrated

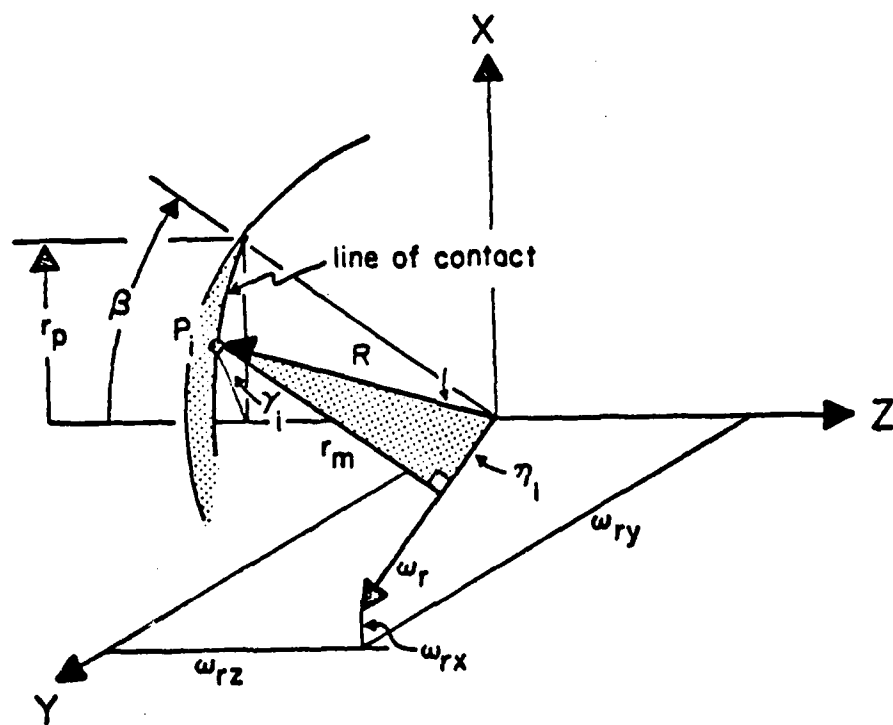


Figure 5. Sketch illustrating the location of points of contact between ball and projectile.

in Fig. 5, then the position vector may be written

$$\vec{P} = R(\vec{e}_x \sin\beta \cos\gamma + \vec{e}_y \sin\beta \sin\gamma + \vec{e}_z \cos\beta)$$

where  $\vec{e}_x$ ,  $\vec{e}_y$ , and  $\vec{e}_z$  are unit vectors for the inertial coordinates.

The vector of relative angular velocity may be written,

$$\vec{\omega}_r = \vec{e}_x \omega_{rx} + \vec{e}_y \omega_{ry} + \vec{e}_z \omega_{rz}$$

and, since  $\vec{P} \cdot \vec{\omega}_r = R\omega_r \cos\eta$ , we have

$$\eta = \cos^{-1} \left[ \frac{1}{\omega_r} (\omega_{rx} \sin\beta \cos\gamma + \omega_{ry} \sin\beta \sin\gamma + \omega_{rz} \cos\beta) \right] \quad (16)$$

The angle  $\eta$  is that subtended by the position vector  $\vec{P}$  and the relative angular velocity vector  $\vec{\omega}_r$  so that the moment arm  $r_m$  is given by

$$r_m = R \sin\eta \quad (17)$$

and from Eq. (16) we obtain:

$$r_m = R \left[ 1 - \left( \frac{\omega_{rx}}{\omega_r} \sin\beta \cos\gamma + \frac{\omega_{ry}}{\omega_r} \sin\beta \sin\gamma + \frac{\omega_{rz}}{\omega_r} \cos\beta \right)^2 \right]^{\frac{1}{2}} \quad (18)$$

With the point of contact specified the moment arm is therefore determined and, together with the normal force  $F_n$ , leads to the torque due to sliding friction, Eq. (15).

At present it is impossible to exactly specify the vector of the forces applied to the ball. We have therefore examined two special cases that are relevant to the investigation. These are:

1. Motion under a gravity load.
2. Motion under an axial aerodynamic load.

Gravity load. In this case the load is the weight,  $W$ , of the ball and is applied directly downward. The point of contact is at the bottom of the cavity so that  $\beta = \pi/2$  and  $\gamma = \pi$  (that is,  $\vec{P} = -R\vec{e}_x$ ).

The moment arm is given by

$$r_{mg} = R[1 - (\omega_{rx}/\omega_r)^2]^{\frac{1}{2}}$$

and the magnitude of the moment is

$$\bar{M}_{sg} = \mu_s WR [1 - (\omega_{rx}/\omega_r)^2]^{1/2} \quad (19)$$

Which is applied opposite to the relative velocity vector in accordance with Eq. (12).

Axial aerodynamic load. The aerodynamic load acting upon the ball will be a complex function of the ball orientation. During the opening instants, however, when the ball blocks the tubular projectile, the resultant of the pressure forces on the ball will act along the axis of the projectile. This interval is of importance, of course, since it will constitute a significant part of the ball-opening delay. At lower values of  $\theta$ , when there is significant flow through the ball, the specification of the net aerodynamic force will require further detailed analysis. It is important to note further that when the ball is partially open there may be a significant moment acting upon the ball, as well as a centrally directed force. An understanding of the nature of the aerodynamic force under partially-open conditions is a major goal of continuing research.

For the case of an axially oriented applied force, the ball will be forced against the aft rim of the hole in the projectile. The exact number and location of the contact points is difficult to predict and will, in fact, depend upon projectile manufacturing variations. However, any effect of arbitrariness in contact point specification is "blurred" by the high-speed rotary motion and errors resulting should be random and therefore of little influence on the overall motions. This hypothesis has been verified by computer experiments. In selecting the number of contact points and their location, we have assumed the first stable position, that is, three contact points. In addition, we have assumed that these points are symmetrically dispersed along the line of contact.

The axial aerodynamic force,  $F_a$ , is evenly balanced among the contact points so that at each point the normal force is given by

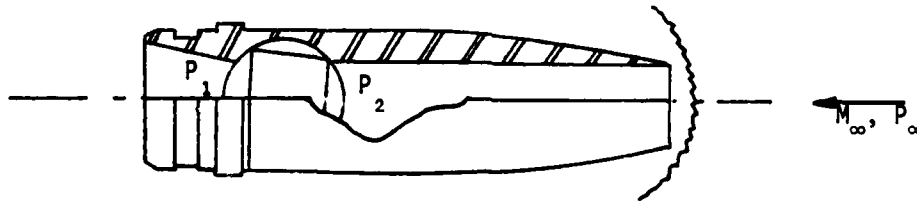
$$F_n = \frac{F_a}{3} \cos \beta$$

and, since the contact points lie along the rim of the projectile hole,  $\beta = \sin^{-1} r/R$ . (see Fig. 5). The moment due to sliding friction in this case is given by

$$M_{sa} = \mu_s (F_a/3) \cos \beta \sum_{i=1}^3 (r_m)_i \quad (20)$$

where  $\beta = \sin^{-1}(r/R)$  and the three values of  $r_m$  are given by Eq. (18) with the angle  $\gamma$  set at 0,  $2\pi/3$ , and  $4\pi/3$ .

The aerodynamic force most appropriate for use in Eq. (20) will be that due to a pressure distribution over the ball and behind a normal shock standing at the projectile entrance. (see sketch below)



The net force on the ball will be

$$F_a = \pi r^2 (P_2 - P_1)$$

Since the actual base pressure  $P_1$  is much less than  $P_2$  and, in any case, is unknown, we assume ambient pressure here. That is,  $P_1 \approx P_\infty$ . The face

$P_2$  will lie somewhere between the static and the stagnation pressure existing behind the shock. The difference is small (about 7%) in the range of Mach numbers of interest ( $M_\infty = 3$  to 5) and will likely approach the static pressure because of spillage behind the shock and recirculation within the cavity ahead of the ball; that is, there will be little or no pressure recovery in the cavity. The assumption of static pressure is adopted for these reasons as well as the fact that this is a conservative assumption in terms of ball opening times (higher pressures lead to shorter opening times). Thus, the approximate expression for the pressure  $P_2$  is

$$P_2 = P_\infty \left[ 1 + \frac{2k}{k+1} (M_\infty^2 - 1) \right]$$

and for the aerodynamic force,

$$F_a = \pi r^2 P_\infty \left[ \frac{2k}{k+1} (M_\infty^2 - 1) \right] \quad (21)$$

Equations (20) and (21) provide the necessary information for determining the torque due to an axial aerodynamic load and this torque is, again, applied in a direction opposite to that of the relative velocity vector.

#### Consideration of the Relative Angular Velocity Vector

The three body-fixed components of the relative velocity vector are given by see Eqs. (5) :

$$\begin{aligned} \omega_{1r} &= (\dot{\psi} - \omega_p) \sin\theta \sin\phi + \dot{\theta} \cos\phi \\ \omega_{2r} &= (\dot{\psi} - \omega_p) \sin\theta \cos\phi - \dot{\theta} \sin\phi \\ \omega_{3r} &= (\dot{\psi} - \omega_p) \cos\theta + \dot{\phi} \end{aligned} \quad (22)$$

According to Eq. (12), then, the components of the external moments may be written:

$$\begin{aligned} M_1 &= - \frac{\bar{M}}{A \omega_{po}^2 \bar{\omega}_r} [(\dot{\psi} - \omega_p) \sin\theta \sin\phi + \dot{\theta} \cos\phi] \\ M_2 &= - \frac{\bar{M}}{A \omega_{po}^2 \bar{\omega}_r} [(\dot{\psi} - \omega_p) \sin\theta \cos\phi - \dot{\theta} \sin\phi] \\ M_3 &= - \frac{\bar{M}}{C \omega_{po}^2 \bar{\omega}_r} [(\dot{\psi} - \omega_p) \cos\theta + \dot{\phi}] \end{aligned} \quad (23)$$

The terms involving these moments in the equations of motion may now be written

$$\begin{aligned} M_1 \sin\phi + M_2 \cos\phi &= \frac{-\bar{M}}{A\omega_{po}^2 \bar{\omega}_r} [(\dot{\psi} - \omega_p) \sin\theta] \\ M_1 \cos\phi - M_2 \sin\phi &= \frac{-\bar{M}}{A\omega_{po}^2 \bar{\omega}_r} \ddot{\theta} \end{aligned} \quad (24)$$

$M_3$  = as in Eq. (23).

The value of  $\bar{M}$  in these expressions are given according to the table below:

<u>Source of moment</u>	<u>Applicable Equations</u>
Fluid Shear, $\bar{M}_f$	(14)
Sliding Friction	
Gravity only, $\bar{M}_{sg}$	(19)
Axial Aerodynamic, $\bar{M}_{sa}$	(20, 21)

It is appropriate to combine the fluid shear moment with either of the sliding friction moments. In most cases analyzed, however, fluid shear moments are several orders of magnitude smaller than those due to sliding friction. Since the gravity and axial aerodynamic loads are each dependent upon specified points of contact, it is not appropriate to combine them without determining a point of contact that is correct for the combination. In cases of practical interest, however, the aerodynamic load is either absent or, if it is present, it completely dominates any effects due to gravity. Consider, for instance, a sea level launch under the following conditions:

$$r = 4.7 \text{ mm}$$

$$R = 7.9 \text{ mm}$$

$$M_{\infty} = 3.0$$

Under the approximation that the moment arms are about equal to the sphere

radius for both gravity and aerodynamic loads, the ratio of moments for the two cases is

$$\frac{M_{sg}}{M_{sa}} \approx \frac{W}{F_a}$$

For the stated conditions with a steel ball,  $W \approx .08 \text{ N}$  (about 0.4 lb.) and  $F_a \approx 65 \text{ N}$  (about 15 lb.) so that the aerodynamic effect is clearly dominant.

It should be noted, in closing this section, that the main weakness in the analysis is due to uncertainties in specifying the aerodynamic load. If this load (force vector or centrally applied force plus moment) is known, the methods given to predict its affect upon the motion are quite general.



## EXACT SOLUTIONS FOR TYPICAL SYSTEM PARAMETERS

Equations (8) - (10), subject to the initial conditions [Eq. (11)] have been solved for both the gravity-only case and the case of an axial aerodynamic load. The gravity-only case is of special interest because it provides theoretical predictions for the experimental program (described in a subsequent section). The aerodynamic load is, of course, the practical case for the tubular projectile.

The appropriate equations were coded for solution on the digital computer. The general flow of the solution method is as follows:

1. Set initial conditions and specify system parameters.
2. Calculate necessary constants (ball weight, moments of inertia, flight level pressure, etc.).
3. Calculate  $\omega_1, \omega_2, \omega_3$  from current Euler angles [Eqs. (5)].
4. Calculate body-fixed components of relative angular velocity [Eqs. (22)].
5. Convert relative angular velocity components to inertial axes ( $\omega_{rx}, \omega_{ry}, \omega_{rz}$ ).
6. Determine moment arms and external moments as required (see table, p. 22).
7. Determine moment terms, for use in equation of motion [Eqs. (24)].
8. Determine  $\ddot{\psi}, \ddot{\theta},$  and  $\ddot{\phi}$  [Eqs. (8) - (10)].
9. Integrate for new values of  $\dot{\psi}, \dot{\theta}, \dot{\phi},$  and  $\psi, \theta,$  and  $\phi$ .
10. Return to step 3, until  $\theta$  is sufficiently close to zero.

The method of integration employed (step 9 above) was a fourth-order Runge-Kutta scheme with a step-size automatically adjusted to control numerical precision.

### Consideration of Projectile Angular Velocity.

Two system constraints have been investigated in the analysis. In the first case we have invoked the constraint of constant projectile spin rate and, in the second case, we have required a constant system (ball plus projectile) kinetic energy. Since the inertia of the ball is small relative to that of the projectile (a factor of about 20) the decrease in projectile spin rate necessary to maintain constant system kinetic energy during the ball motion is rather small (typically about 2%) and the two cases are not significantly different. The computer solutions shown here (so-called "exact" solutions) are for the case of constant system kinetic energy.

### Gravity Load.

The system parameters for this case were set to correspond to the conditions of the experiments to be described later. These parameters are summarized in Table I.

Figures 6 and 7 illustrate the nature of the motion predicted by the exact solutions for a representative set of the physical parameters. In Fig. 6 the angle of tilt ( $\theta$ ) relative to the cavity spin axis is shown as a function of time for various rates of spin. At relatively high rates of spin the motion appears to be quite linear with a nearly constant rate of nutation ( $\dot{\theta}$ ) developed early in the motion. At lower rates of spin, however, there is an initial period during which the motion is nearly stable, followed by a rapid decrease in the tilt angle. The time required to reach a given value of  $\theta$  is therefore a function of the angle itself and is illustrative of the complex interactions between the inertial tendencies of the ball and the dissipative torques due to friction. Figure 7 is included to show the variations in the Euler angle rates for a typical case. When the ball is released its rate of precession

TABLE I

## Ball Characteristics and Experimental Conditions - Gravity Load

Ball Designation	Mod 0	Mod I
<u>Physical Characteristics</u>		
R, m	$7.899 \times 10^{-3}$	$7.925 \times 10^{-3}$
r, m	$4.722 \times 10^{-3}$	$1.984 \times 10^{-3}$
C, Nms <sup>2</sup>	$3.126 \times 10^{-7}$	$4.029 \times 10^{-7}$
$\lambda$	0.410	0.077
$\rho$ , kg/m <sup>3</sup>	$7.67 \times 10^3$	$7.75 \times 10^3$
<u>Experimental Conditions</u>		
$\mu$ , Ns/m <sup>2</sup>	$1.917 \times 10^{-5}$	$1.917 \times 10^{-5}$
$\mu_s$ (note 1)	0.51	0.30
$\epsilon$	$6.43 \times 10^{-5}$	$6.43 \times 10^{-5}$
$\theta_o$ , deg	87.25	89.5
$\theta^*$ , deg	36.71	14.50
$\bar{M}$ , Nm (note 2)	$2.08 \times 10^{-4}$	$2.18 \times 10^{-4}$

<sup>1</sup>Empirically determined, see text.

<sup>2</sup>Computed from Eq. (39).

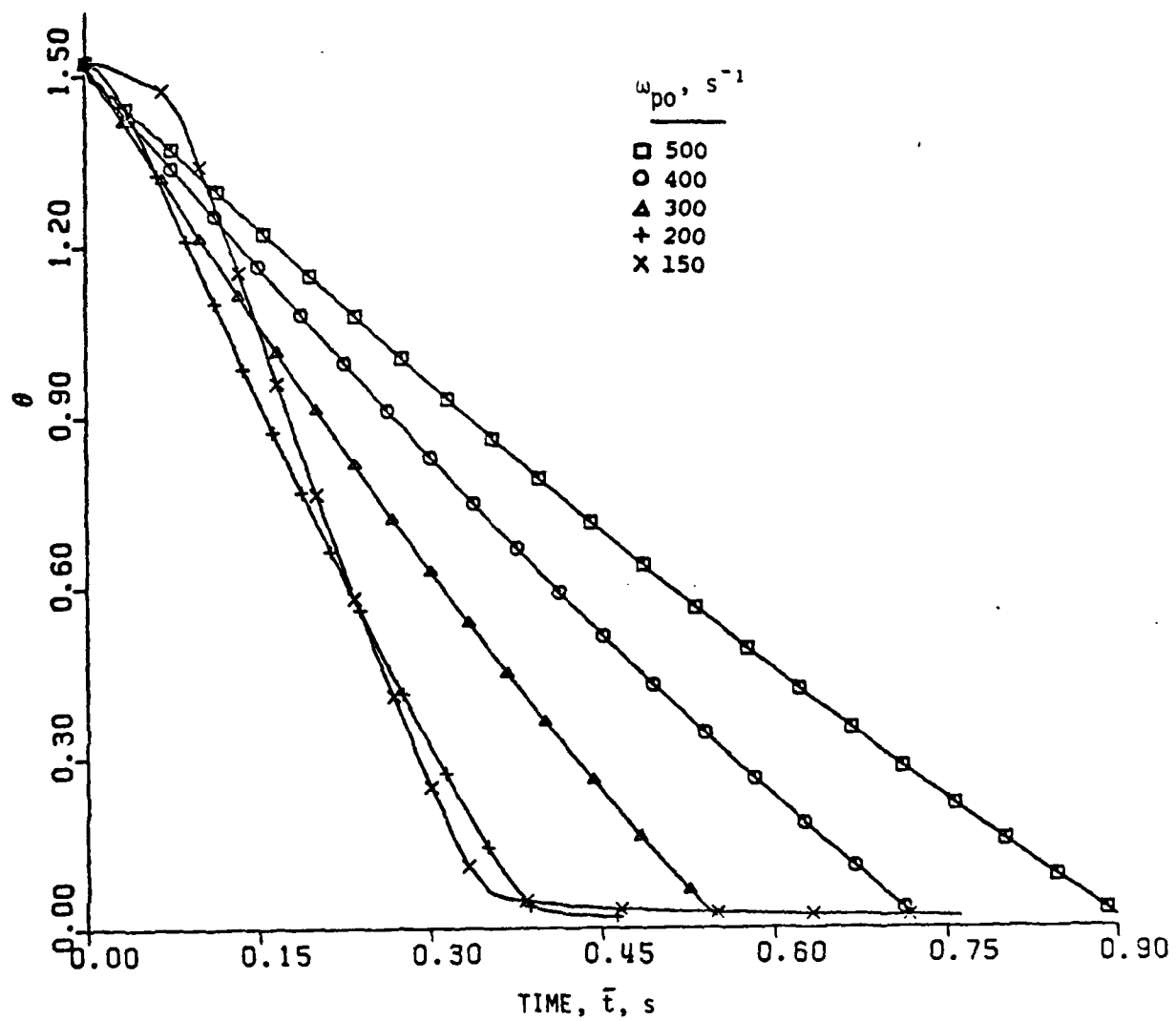


Figure 6. Exact solutions for  $\theta$  vs  $\bar{t}$ . Gravity load only; ball Mod 0.

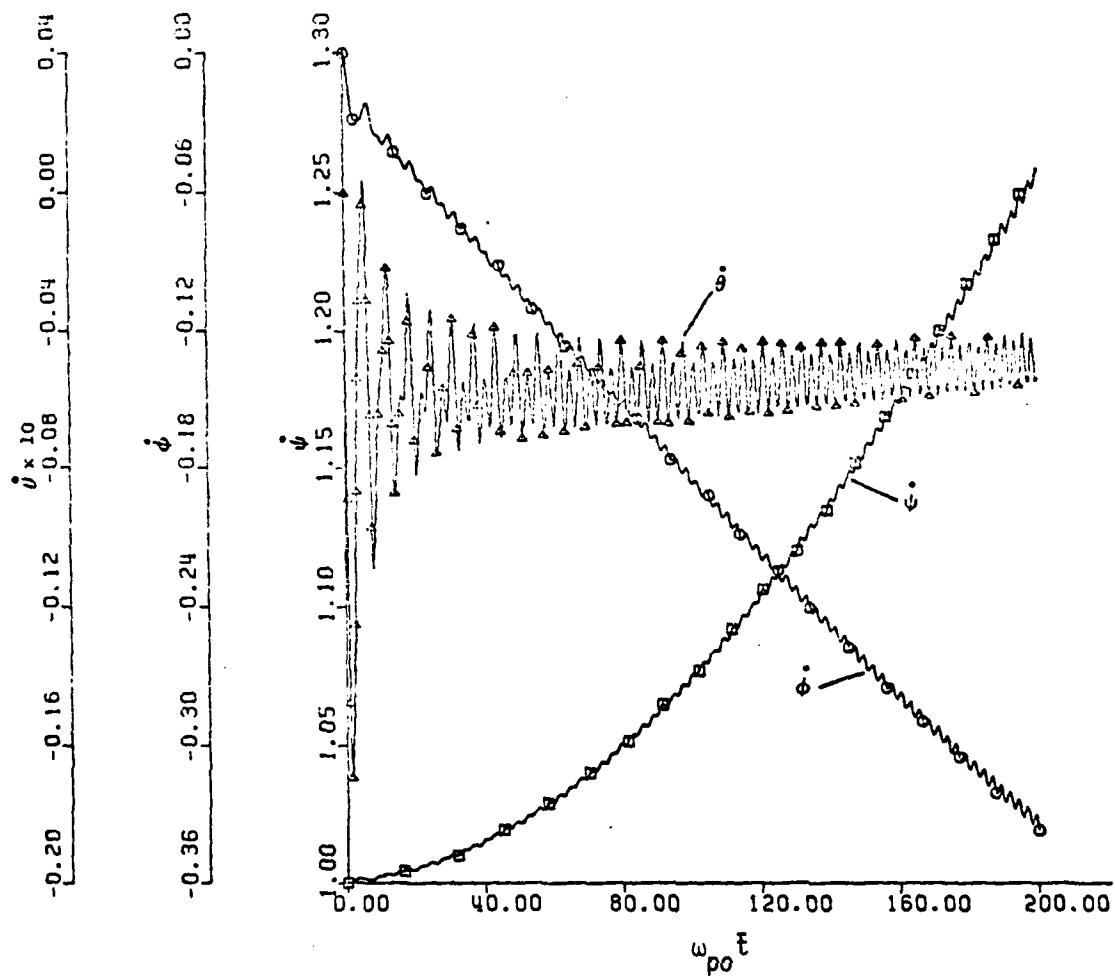


Figure 7. Euler angle rates (non-dimensional) for typical case. Gravity load only, ball Mod 0,  $\omega_{po} = 400 \text{ s}^{-1}$ .

$(\dot{\psi})$  increases above its initial non-dimensional value of unity and, concurrently, a retrograde spin is developed. For the conditions of Fig. 7 ( $\omega_{p0} = 400\text{s}^{-1}$ ), the mean value of nutation rate is fairly constant with acceleration rates that are initially large and rapidly damped. Additional results for case of gravity load are discussed in conjunction with the linear approximation and experimental results.

#### Axial Aerodynamic Load.

Figures 8 and 9 present similar results for the motion under an aerodynamic load. The system parameters for these figures are those of the "baseline case" listed in Table II.

The nature of the response is seen to be similar to that of the gravity-only case. In particular, the existence of a hovering mode is apparent at low projectile spin rates. This phenomenon points up some design limits and is the subject of discussion in a subsequent section. Sensitivity studies were conducted for the aerodynamic load and these also are discussed later.

TABLE II

## Ranges of Design Variables - Aerodynamic Load

Design Variable	Minimum	Baseline	Maximum	Figure No. <sup>1</sup>
R, mm	baseline	7.90	39.5	24
A, Nms <sup>2</sup>		$2.24 \times 10^{-7}$	$7.00 \times 10^{-4}$	
r/R	0.400	0.598	0.800	25
A, Nms <sup>2</sup>	$3.20 \times 10^{-7}$	$2.24 \times 10^{-7}$	$1.00 \times 10^{-7}$	
$\lambda$	0.19	0.41	0.69	
$\rho$ , kg/m <sup>3</sup>	$3.10 \times 10^3$	$7.75 \times 10^3$	$1.24 \times 10^4$	26
A, Nms <sup>2</sup>	$8.96 \times 10^{-8}$	$2.24 \times 10^{-7}$	$3.58 \times 10^{-7}$	
$\mu_s$	0.71	0.855	1.000	27
$M_\infty$	3.00	3.50	5.00	28
$P_\infty$ , atm	0.1	1.0	baseline	29
$\omega_{po}$ , s <sup>-1</sup>	$6.91 \times 10^3$	$1.20 \times 10^4$	$1.36 \times 10^4$	8
$\theta_o$ , deg	70	85	baseline	8, 10

<sup>1</sup> Figures cited are those in which the given design variable is investigated over a range of values.

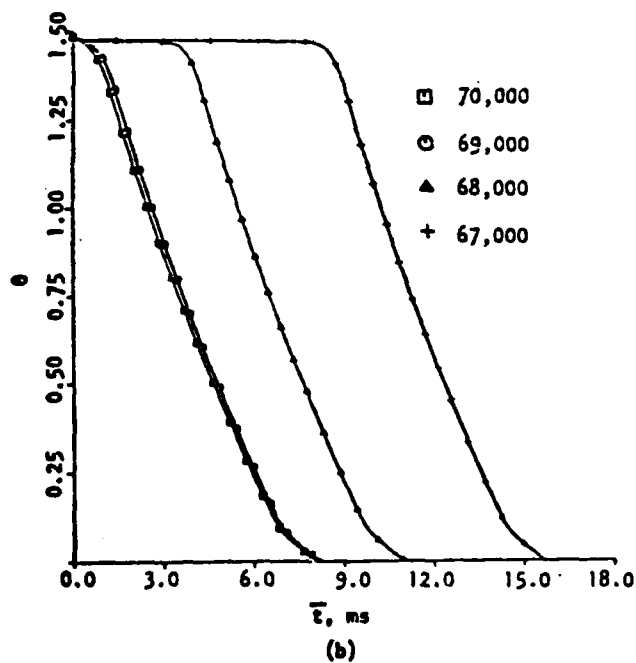
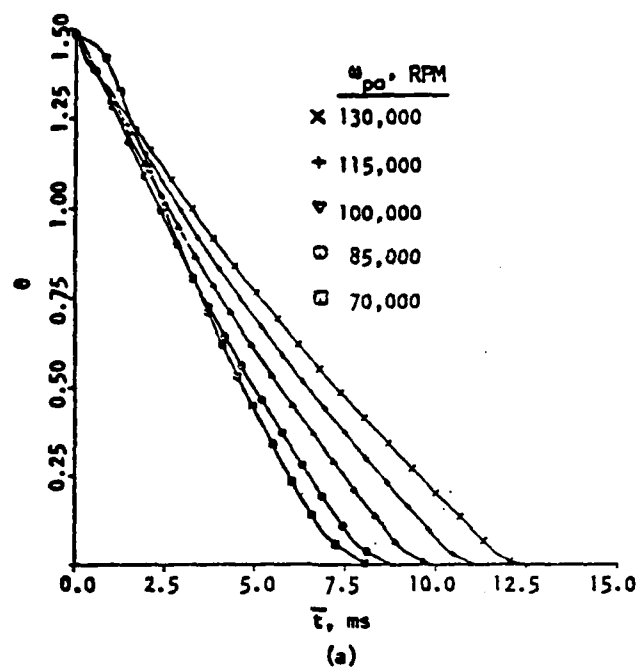


Figure 8. Exact solutions for  $\theta$  vs  $\bar{\tau}$ ; baseline projectile. (a) High projectile spin rates; (b) low projectile spin rates.



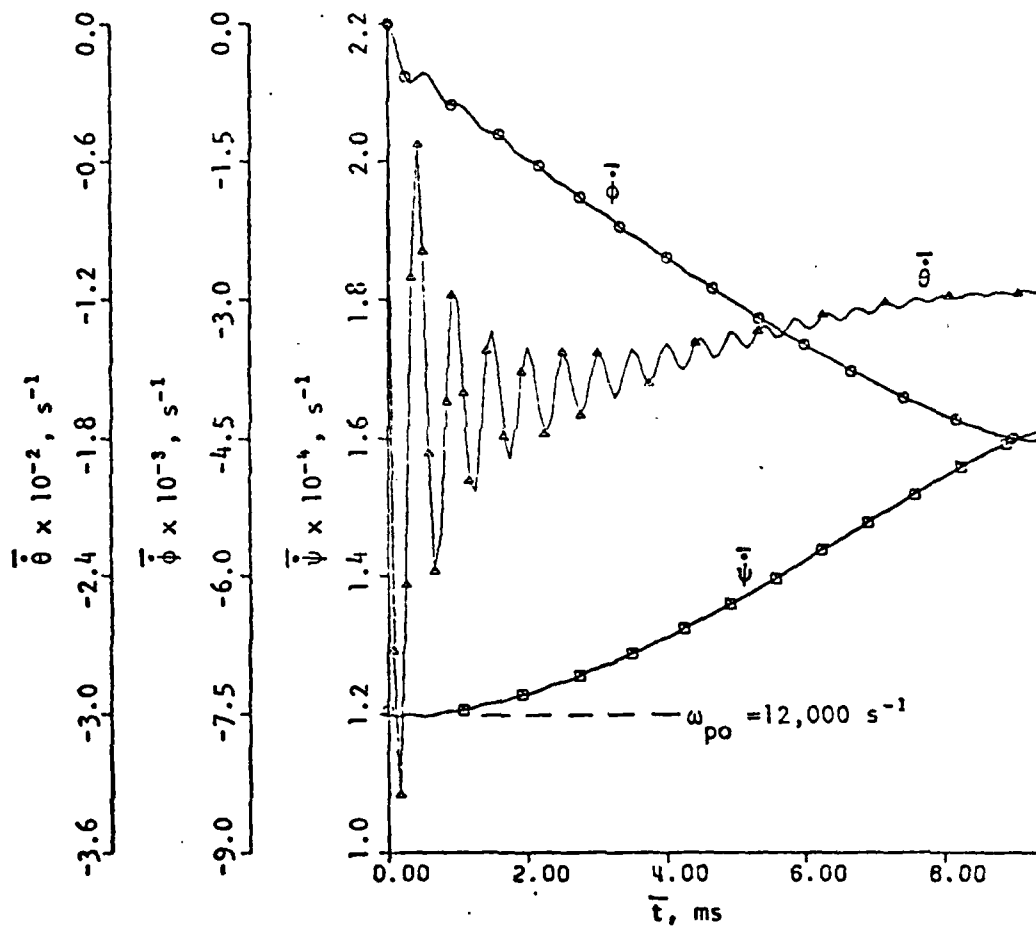


Figure 9. Euler angle rates for a typical case. Baseline projectile,  $\omega_{po} = 1.20 \times 10^4 \text{ s}^{-1}$  (115,000 rpm).

### LINEAR APPROXIMATIONS

From Figs. 8a and 8b it will be noted that there is a marked change in the nature of the ball motion at a projectile spin rate of about  $7300 \text{ s}^{-1}$  (70,000 rpm). At rates above this value (Fig. 8a) the ball motion appears to be quite linear; that is, the response of the ball to the frictional torques approximates one of a second-order linear system responding to a combined ramp and step input (both of which are negative). Such a response is given by

$$\theta = \theta_0 + D + R(t - 2\zeta) \dots \quad (25)$$

$$+ \exp(-\zeta t) \{ R \sin[(1-\zeta^2)^{1/2} t + \phi_R] - D \sin[(1-\zeta^2)^{1/2} t + \phi_D] \} / (1-\zeta^2)^{1/2}$$

where  $\phi_D = \phi_R/2 = \tan^{-1}[(1-\zeta^2)^{1/2}/\zeta]$

The parameters of the response, to be derived below, are given by:

$$\zeta = M/2, \quad D = -(\lambda/2) \sin 2\theta_0, \quad \text{and} \quad R = MD/(\lambda + 1)$$

The method leading to the linear approximation is a perturbation upon the equilibrium solution to Eqs. (8) - (10) under torque-free conditions.

#### DEVELOPMENT OF THE PARAMETERS OF THE LINEAR RESPONSE

Equation (25) satisfies the initial conditions on  $\theta$  and is the solution to

$$\ddot{\theta} + 2\zeta\dot{\theta} + \theta = \theta_0 + D + Rt \quad (26)$$

From the equations of motion for  $\ddot{\theta}$  and the associated relation for external moment [Eqs. (9) and (24)], a comparison of the coefficient of the tilt velocity,  $\dot{\theta}$ , leads to the damping coefficient:

$$\zeta = M/2 \quad (27)$$

where  $M = \bar{M}/A\omega_{po}\bar{\omega}_r$ .

With this definition of  $\zeta$ , combination of Eqs. (9) and (26) leads

to

$$(\theta - \theta_0) - (D + Rt) = \dot{\psi} \sin \theta [(\lambda + 1)\dot{\phi} + \lambda \dot{\psi} \cos \theta] \quad (28)$$

The response specified in Eq. (25) indicates that the function described in Eq. (28) is oscillatory in nature with the mean value decaying exponentially from an initial value of  $-D$  to an asymptotic final value of  $-2R\zeta$ . That is, the mean value (about which the oscillations occur) is given by:

$$[(\theta - \theta_0) - (D + Rt)]_{\text{mean}} = -2R\zeta - (D - 2R\zeta)\exp(-\zeta t)$$

In the limiting case of vanishingly small external moments this expression simplifies to a straight-line response with slope  $R$  so that an evaluation of this rate of decay should emerge from an investigation of the solution of the equations of motion for the case of zero external moments.

If the external moments are removed from Eqs. (8) - (10), a solution of the following form is obtained:

$$(\lambda + 1)\ddot{\phi}_0 + \lambda \cos \theta_0 = 0, \quad \dot{\theta}_0 = 0, \quad \dot{\psi}_0 = 1 \quad (29)$$

The subscript  $(_0)$  is used here to indicate quantities pertaining to this solution. Perturbations to this solution, designated by subscript  $(_p)$ , are defined such that

$$\begin{aligned} \psi &= \psi_0 + M\psi_p \\ \phi &= \phi_0 + M\phi_p \\ \theta &= \theta_0 + M\theta_p \end{aligned} \quad (30)$$

The base quantities (subscript  $o$ ) must satisfy Eq. (29) and the perturbed quantities (no subscript) must satisfy the initial conditions, Eq. (11). The appropriate initial conditions for the perturbations are, therefore

$$\begin{aligned} \dot{\psi}_p(0) &= 0 \\ \dot{\phi}_p(0) &= -\dot{\phi}_0/M = -\lambda \cos \theta_0 / M(\lambda + 1) \\ \theta_p(0) &= \dot{\theta}_p(0) = 0 \end{aligned} \quad (31)$$

When Eqs. (29) and (30) are inserted into Eqs. (8) and (10), the following approximate relationships are obtained:

$$M\ddot{\psi}_p \sin\theta_0 = T_1 - M\dot{\theta}_p \cos\theta_0 + O(M^2)$$

$$M\ddot{\phi}_p = T_2 + M\dot{\theta}_p \sin\theta_0 - M\ddot{\psi}_p \cos\theta_0 + O(M^2)$$

where the torque terms  $T_1$  and  $T_2$  are obtained from Eqs. (24), (29), and (30):

$$T_1 = -M(M\dot{\psi}_p \sin\theta_0) = O(M^2)$$

$$T_2 = -M\dot{\phi}_0/(\lambda + 1) + O(M^2)$$

Neglecting terms of order  $M^2$  and smaller, we have

$$\ddot{\psi}_p \sin\theta_0 = -\dot{\theta}_p \cos\theta_0$$

$$\ddot{\phi}_p = -\dot{\phi}_0/(\lambda + 1) + \dot{\theta}_p \csc\theta_0$$

The first integrals of this set yield

$$\dot{\psi}_p = -\theta_p \cot\theta_0$$

$$\dot{\phi}_p = -\dot{\phi}_0 t/(\lambda + 1) + \theta_p \csc\theta_0 - \dot{\phi}_0/M \quad (32)$$

or, from Eqs. (30)

$$\dot{\psi} = 1 - M\theta_p \cot\theta_0$$

$$\dot{\phi} = -M\dot{\phi}_0 t/(\lambda + 1) + M\theta_p \csc\theta_0 \quad (33)$$

When Eqs. (29) and (30) are substituted into Eq. (28) we have, to the first order:

$$M \sin\theta_0 [(\lambda + 1)\dot{\phi}_p + \lambda\dot{\psi}_p \cos\theta_0 - \lambda\theta_p \sin\theta_0] = M\theta_p - (D + Rt)$$

and with Eqs. (32) this becomes

$$(\lambda + 1) \sin\theta_0 [M\dot{\phi}_0 t/(\lambda + 1) + \dot{\phi}_0] = D + Rt$$

It follows that:

$$D = (\lambda + 1)\dot{\phi}_0 \sin\theta_0 = -(\lambda/2) \sin 2\theta_0 \quad (34)$$

$$R = MD/(\lambda + 1)$$

In order to evaluate the non-dimensional moment parameter,  $M$ , it is necessary to develop approximate relationships for  $\omega_r$  and for the moment arm  $r_m$  to be used in the previously derived expressions. Under the constraints of the linearization described here ( $M \ll 1$  and  $|D| \ll 1$ ), the relative angular velocity is approximated by [Eqs. (22)]:

$$\omega_r \approx \omega_{3r} \approx \dot{\phi}_0 = -\lambda \cos \theta_0 / (\lambda + 1)$$

The principal component of the relative angular velocity is therefore along the spin axis of the ball and, since the ball is initially near  $\theta_0 = \pi/2$  (required for  $|D| \ll 1$ ) the components along the inertial axes are, approximately,

$$\omega_{rx}/\omega_r \approx \sin \psi_0$$

$$\omega_{ry}/\omega_r \approx \cos \psi_0$$

$$\omega_{rz}/\omega_r \approx 0$$

Since  $\psi_0$  is a function of time (even though  $\dot{\psi}_0 = \text{constant} = 1$  in the linearization), suitable mean values for the moment arm relationships must be obtained. In the case of a gravity-only load we have

$$r_{mg} = R[1 - (\omega_{rx}/\omega_r)^2]^{1/2} = R|\cos \psi_0|$$

the absolute value being necessary to preserve the positive nature of the moment arm. For the mean value,

$$\bar{r}_{mg} = \frac{1}{2\pi} \int_0^{2\pi} r_{mg} d\psi_0$$

we have

$$\bar{r}_{mg} = \frac{1}{2\pi} \int_0^\pi R|\cos \psi_0| d\psi_0 = \frac{2R}{\pi} \int_0^{\pi/2} \cos \psi_0 d\psi_0$$

and

$$\bar{r}_{mg} = (2/\pi)R \quad (36)$$

For the case of aerodynamic loads, we have from Eq. (18)

$$r_{ma} = R[1 - \sin^2 \beta \sin^2(\psi_0 + \gamma)]^{1/2}$$

where the selected values of  $\psi_0$  locate the contact points and  $\beta = \sin^{-1}(r/R)$ .

In the mean, then

$$\bar{r}_{ma} = \frac{2R}{\pi} \int_0^{\pi/2} [1 - \sin^2 \beta \sin^2(\psi_0 + \gamma)]^{1/2} d\psi_0$$

and

$$\bar{r}_{ma} = (2/\pi)R E(\beta) \quad (37)$$

where  $E(\beta)$  is the Complete Elliptic Integral of the second kind.

With these values for the moment arms it remains to evaluate the linearized forms of the external moments. In the case of fluid friction we have, from Eq. (14),

$$M_f = [8\pi(1 + \epsilon)\mu R^3 \bar{\omega}_r / (3\epsilon)] / A \bar{\omega}_r \omega_{po}$$

or

$$M_f = 8\pi(1 + \epsilon)\mu R^3 / (3\epsilon A \omega_{po}) \quad (38)$$

Note that no linearization is required for this non-dimensional moment parameter. For the case of gravity-only loads, from Eq. (19)

$$M_{sg} = [\mu_s W R (2/\pi)] / A \bar{\omega}_r \omega_{po}$$

or

$$M_{sg} = 2\mu_s W R (\lambda + 1) / \pi A \lambda \omega_{po}^2 \cos \theta_0 \quad (39)$$

For the aerodynamic load Eq. (37) gives, for three contact points symmetrically disposed,

$$\sum_{i=1}^3 \bar{r}_{mi} = 3(2/\pi)R E(\beta)$$

and from Eq. (20)

$$M_{sa} = \mu_s F_a R (2/\pi) E(\beta) \cos \beta / A \bar{\omega}_r \omega_{po}$$

or

$$M_{sa} = 2\mu_s F_a R (\lambda + 1) E(\beta) \cos \beta / \pi A \lambda \omega_{po}^2 \cos \theta_0 \quad (40)$$

The fluid friction term,  $M_f$ , may be added to either the gravity term,  $M_{sg}$ , or the aerodynamic term,  $M_{sa}$ , to obtain  $M$  and the related parameters  $[\zeta, R, \text{ and } D \text{ from Eqs. (27) and (34)]$ .

#### RESULTS COMPUTED FROM THE LINEAR APPROXIMATIONS

Figure 10 illustrates the linear approximation in comparison with the exact solution for two initial values of  $\theta$  under fluid friction and gravity load. (As mentioned previously, the effects of fluid friction are generally negligible. This observation also applies in the linearization.) Figure 11 gives similar results of the case of an axial aerodynamic load on the ball. It is seen from both figures that good approximations to the exact solution are obtained from the linearization. The approximation departs from the exact solution as time passes and the ball angle decreases. This is to be expected since the terminal phase of the ball motion is not adequately modeled in the linearization. Nevertheless, the linear model provides valuable insights into the nature of the motion and its most influential parameters. It should be noted again that at the lower angles, when an observer would see a sizable opening through the projectile when sighting along its axis, both theoretical models are subject to the possibility of considerable error. This is especially true in the aerodynamic case because of uncertainties in the load description at partially-open conditions.

The results of the linear approximation are discussed further in connection with the experimental program to be described in the next section.

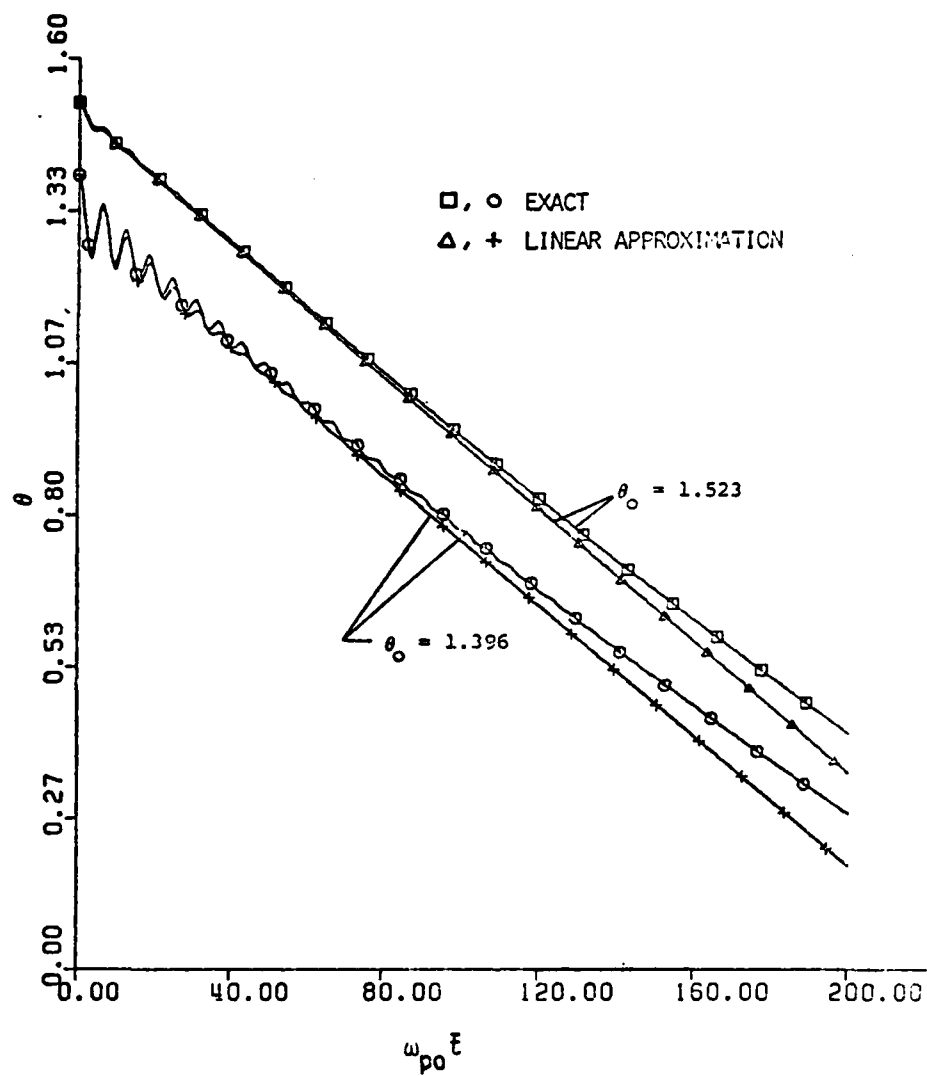


Figure 10. Comparison of approximate solutions with exact solutions. Gravity load only, ball Mod 0,  $\omega_{po} = 400s^{-1}$ .



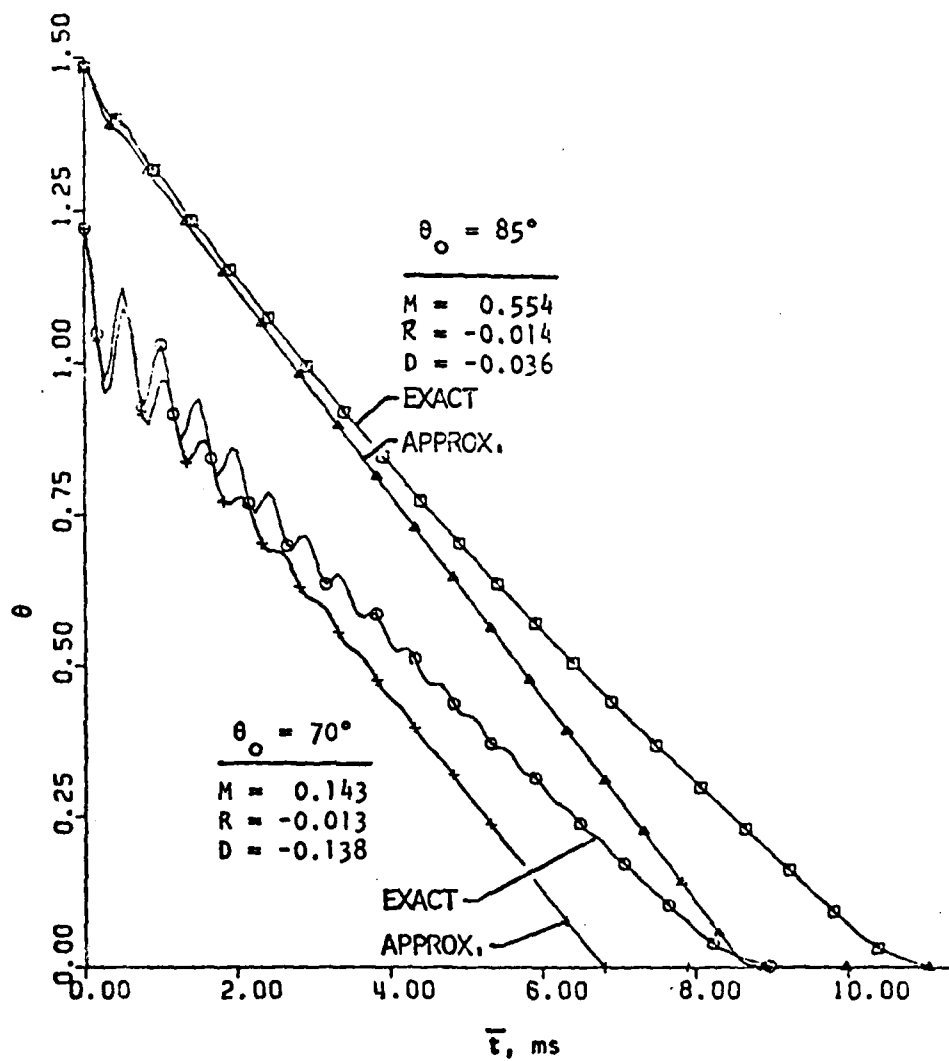


Figure 11. Comparison of approximate solutions with exact solutions.  
 Baseline projectile,  $\omega_{p0} = 1.20 \times 10^4 \text{ s}^{-1}$ .

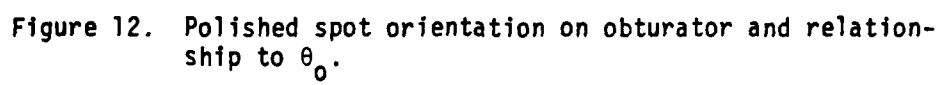
## EXPERIMENTATION

### EXPERIMENTAL APPARATUS

An experimental system was designed to simulate the spinning BOT under the influence of a gravity load. The apparatus consisted of a compressed-air-driven spin-up rig, optical-timing mechanism, air manifold and associated piping, tubing and electronics.

The obturator was fabricated from a standard 5/8-in. diameter chrome-steel (52100) bearing ball. The ball was annealed to allow machining and then bored along a diametrical axis. The bored ball was then mounted in a bakelite metallographic specimen mount. The mounted ball was placed in a milling machine and a flat was machined in the bakelite at a specified angle relative to the axis through the hole in the ball. This flat was then used as the polishing plane for metallographic specimen preparation. A small flat spot was polished on the obturator to provide a highly reflective surface at a known orientation relative to the z-axis of the obturator (Fig. 12).

After removal from the bakelite mount, the obturator was placed in a three-piece, lucite housing (Fig. 13). The mating ends of the two hollow inner cylinders were each machined with a 5/8-inch spherical end mill to a depth of approximately 5/16-inch. When mated, a spherical cavity was formed to accommodate the obturator. The third cylinder was press fit over the others after the obturator was inserted to insure alignment of the inner pieces and provide rigidity (Fig. 14). The ends of this lucite assembly were then press fit into aluminum end-pieces similar to those in Fig. 14. These end-pieces served as the shaft for the bearings and one also served as the prime mover (bucket wheel) for the apparatus. The shaft rotated in two ball bearings mounted in aluminum pillow blocks aligned on a rigid pedestal. The prime mover



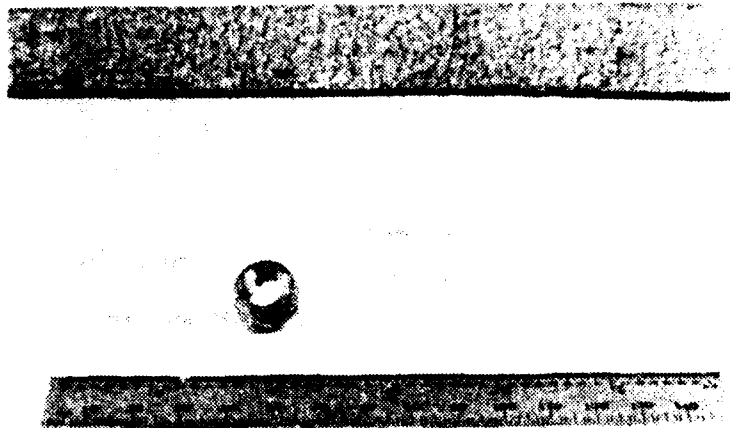


Figure 13. Obturator and components of lucite obturator housing with mating ends of inner cylinders machined to house the obturator.

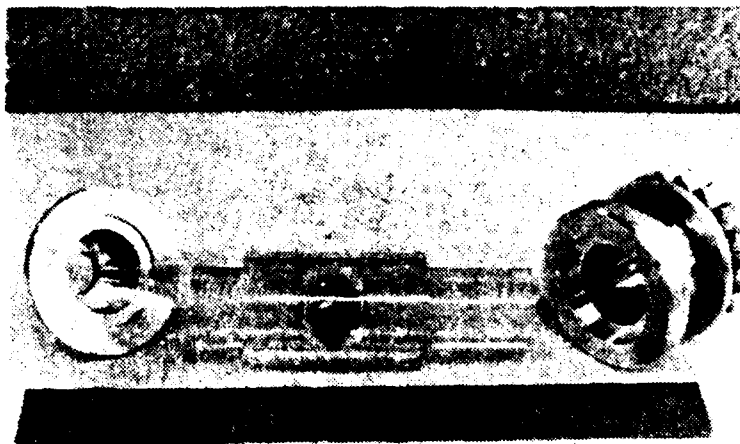


Figure 14. Assembled obturator housing with aluminum end pieces.

was a bucket wheel machined from a solid aluminum disk (Fig. 15).

The bucket wheel was driven by compressed air supplied from an installed system through an air filter to a manifold and then through one of two Model-10 Kendall pressure regulators. From the regulator, the air passed through a flexible tube to a tee, each leg of which supplied a nozzle. These nozzles were mounted opposite one another on the pillow block in such a way as to allow the air jets to impinge upon the bucket wheel to cause rotation (Fig. 16). The speed of rotation was sensed by a Bentley Nevada Proximity, Model 3100N, which was mounted above the bucket wheel to detect the passage of each point on the wheel. The pulses generated by the sensor were counted, averaged and displayed as a frequency by a Monsanto Programmable Counter-Timer Model 110B.

While the spin-up rig was being brought up to the desired speed, an air jet(subsequently referred to as the holding jet) from a nozzle mounted rigidly on the pedestal at the end opposite the bucket wheel held the obturator fixed to the spinning rig. The holding jet passed through a hole in the plunger of a Rocker Solenoid, R.S. No. 10-207. This hole was aligned with the hole through the "projectile" to allow the jet to impinge upon the obturator (Fig. 17). When the appropriate switch was activated, standard 115VAC was applied to the Rocker solenoid and removed from a normally-closed ASCO Solenoid Valve in the air supply line to the holding-jet. The plunger retracted from the position shown in Fig. 17 and the solenoid valve closed. The retraction of the plunger performed three functions. It first caused a pulse to be generated by a proximity mounted next to the nozzle. This pulse started the timer function of a second Model 110B Counter-Timer. The plunger, by misaligning its hole with that of the nozzle, blocked the holding jet. This removed the restraining influence of the holding jet on the obturator and prevented any air

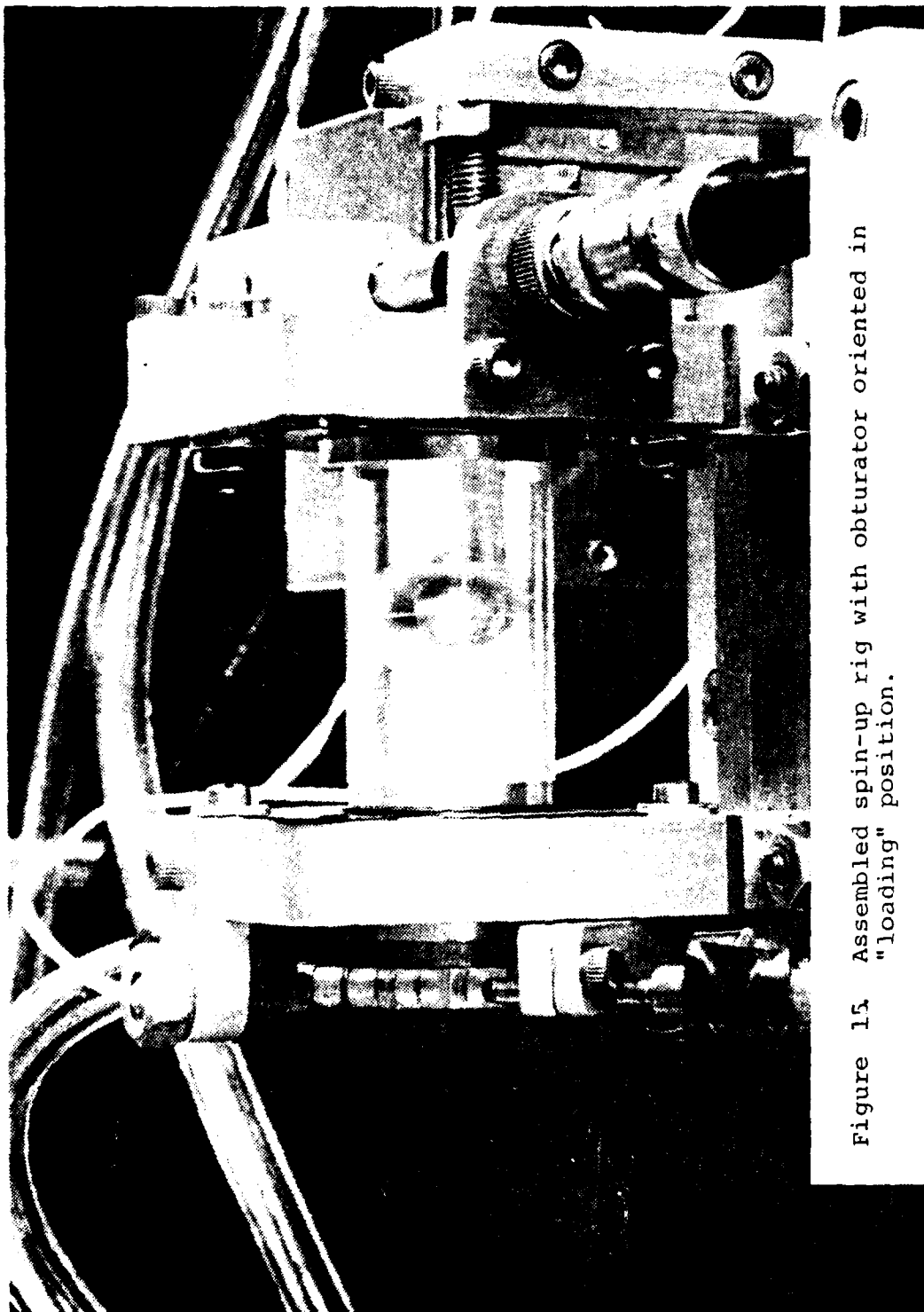


Figure 15 Assembled spin-up rig with obturator oriented in "loading" position.

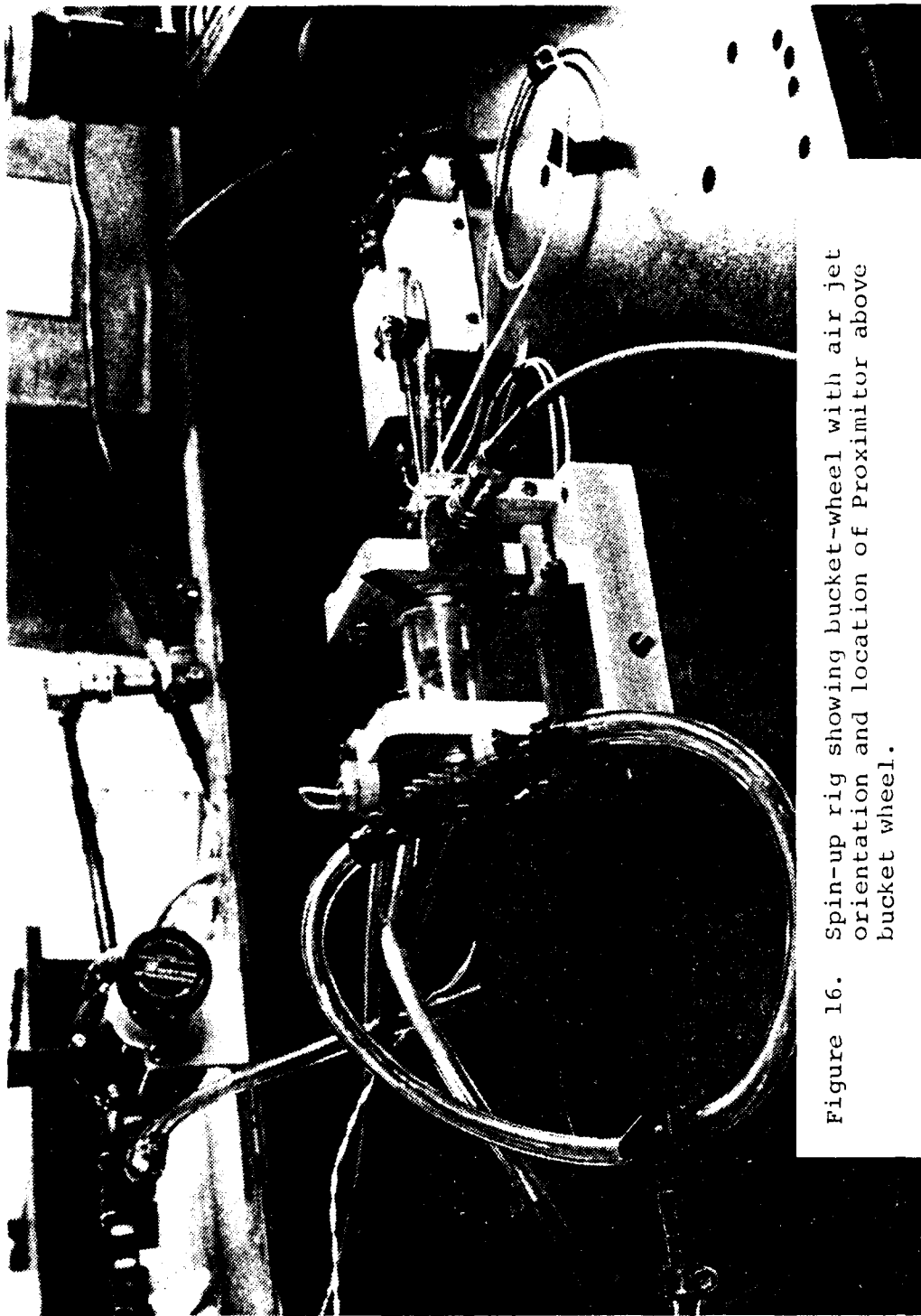


Figure 16. Spin-up rig showing bucket-wheel with air jet orientation and location of Proximator above bucket wheel.

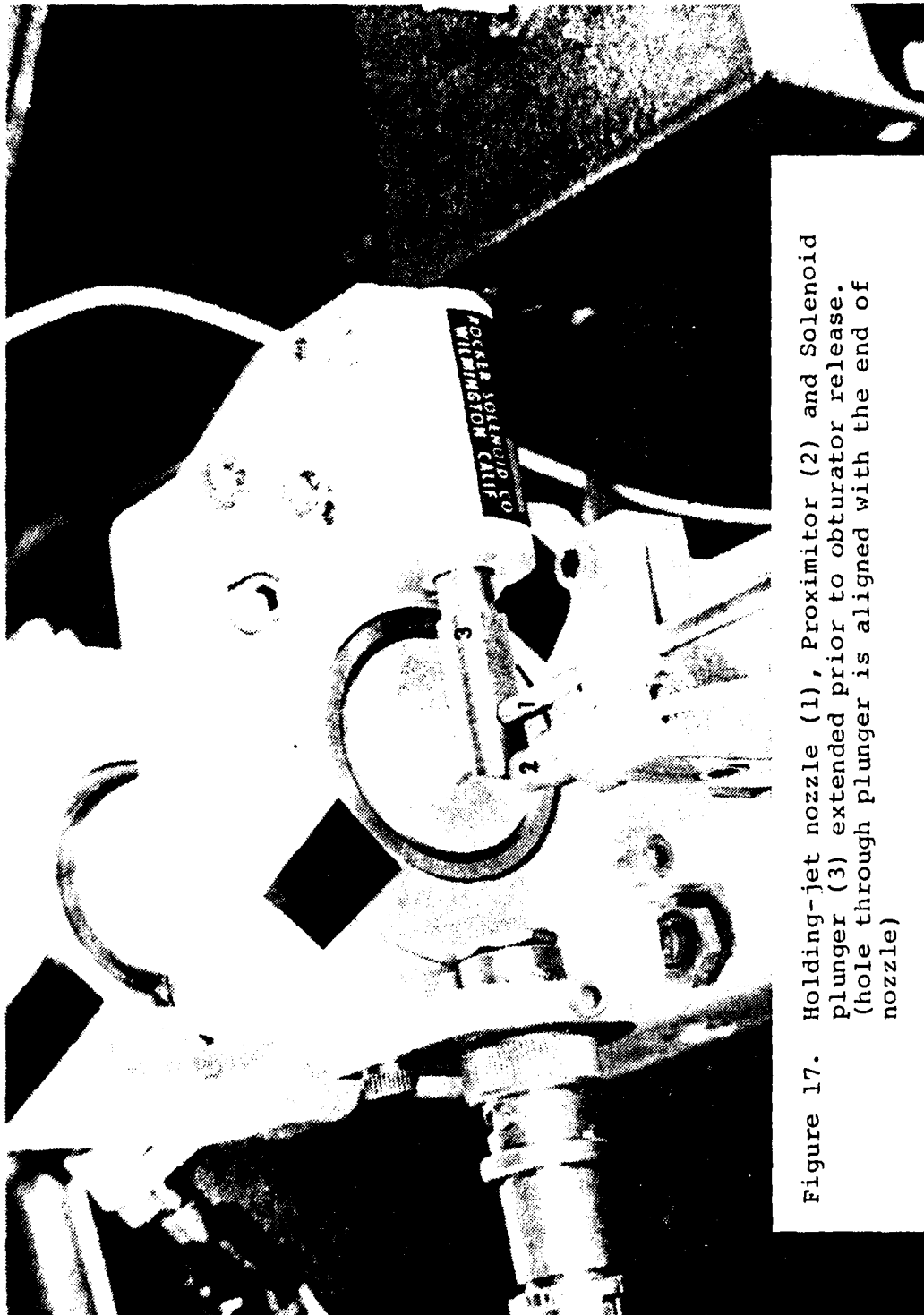


Figure 17. Holding-jet nozzle (1), Proximator (2) and Solenoid plunger (3) extended prior to obturator release. (hole through plunger is aligned with the end of nozzle)

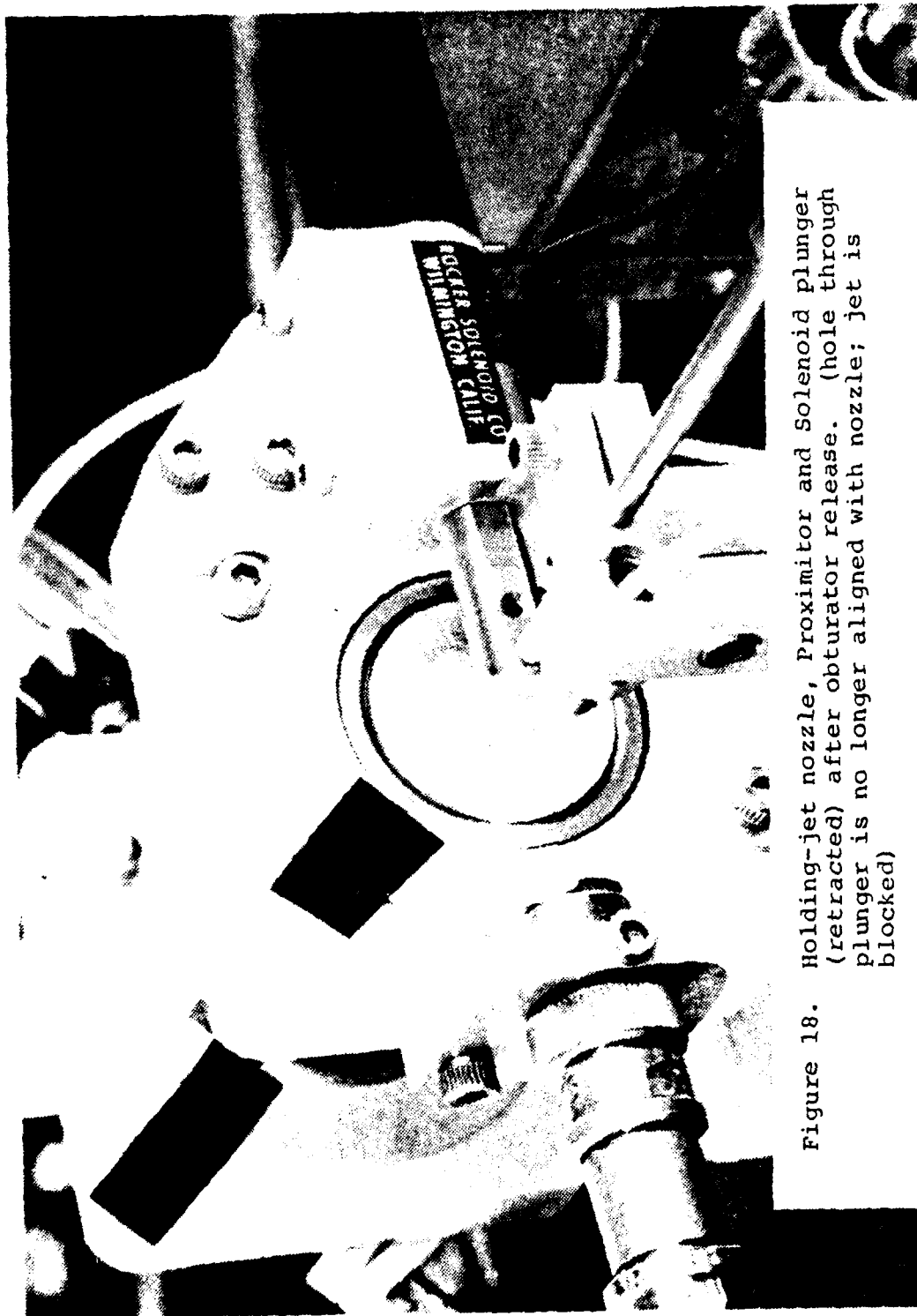


remaining in the supply line from impinging on the obturator. And lastly, in the fully retracted position, the machined and polished end of the plunger was positioned opposite the axis of the apparatus (Fig. 18). When the obturator, now free to move relative to the "projectile", nutated through enough of an angle, the beam of a SPECTRA PHYSICS MODEL 132 LASER, MODEL NO. 3187, passed through the projectile and was reflected by the polished end of the plunger onto a light sensitive diode (Fig. 19). The pulse emitted by the diode triggered the stop channel on the timer and the elapsed time was displayed. Figure 20 shows the entire experimental set-up with air flasks in the background.

#### EXPERIMENTAL PROCEDURE

The obturator was positioned in the spin-up rig in such a way that the laser beam was reflected off the polished spot back to a target mounted on the laser (Figs. 20 and 21). The center of the target is the location of the beam and the obturator was adjusted to place the reflected spot on the center of the target. Thus the orientation of the z-axis through the obturator was known relative to the z-axis (laser beam) through the projectile. This is the initial value  $\theta_0$ .

Once the alignment had been checked and the obturator positioned and held at the known  $\theta_0$ , flow to the turbine nozzles was controlled in such a way that the desired spin rate was achieved. The turbine flow regulator was then adjusted so as to maintain the spin rate at  $\pm 5$  Hz on the digital display or approximately  $\pm 1.75$  rad/sec. Once the desired rate was achieved and noted, and the timer checked and reset if necessary, the solenoid switch (Fig. 17) was activated. The obturator was released and began to move relative to the spin-up rig. When the angle  $\theta$  reached the value at which the laser beam could pass through the obturator hole [ $\theta = \theta^* = \sin^{-1}(r/R)$ ], the beam struck the polished



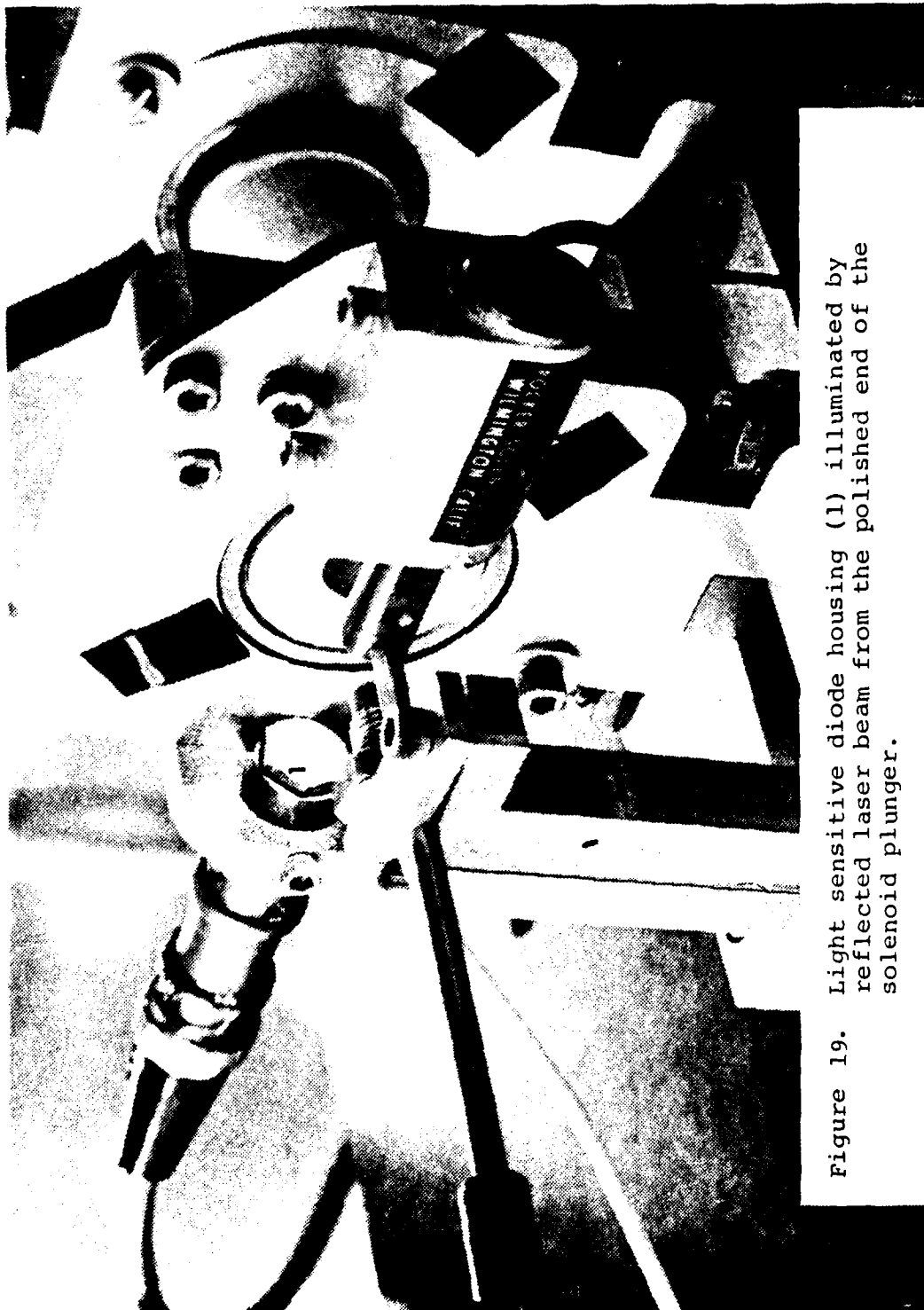


Figure 19. Light sensitive diode housing (1) illuminated by reflected laser beam from the polished end of the solenoid plunger.

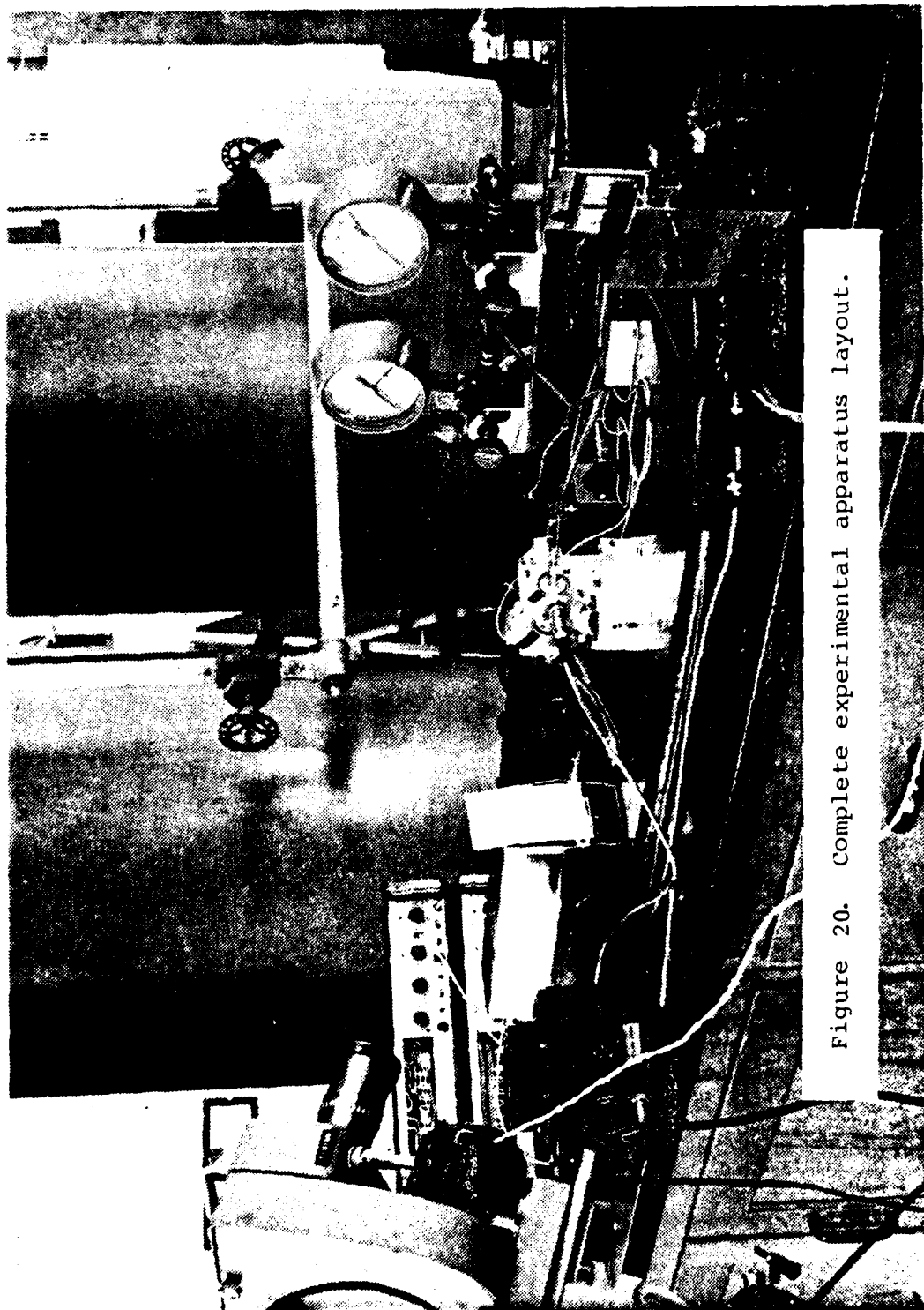


Figure 20. Complete experimental apparatus layout.

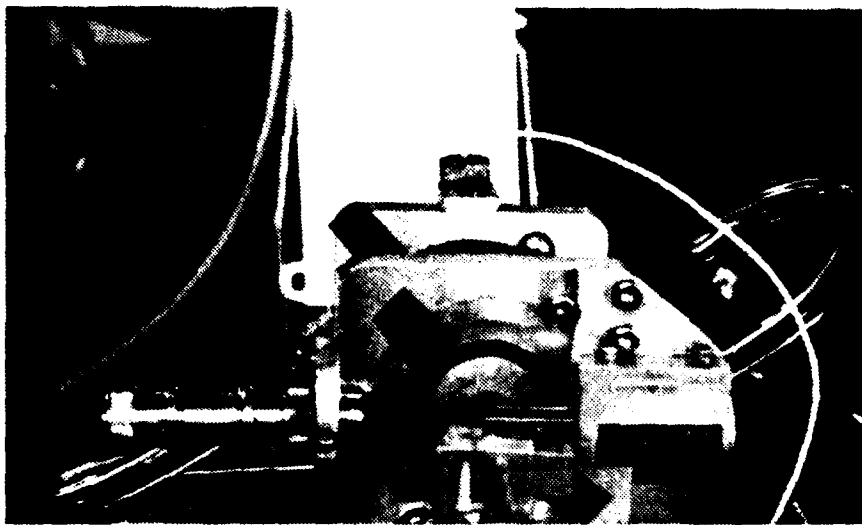


Figure 21. Laser reflection on the target from the polished spot on the obturator.

plunger and was reflected into the light sensitive diode housing. The reflected beam striking the diode caused the diode to emit a pulse which turned off the timer gate. The elapsed time, from plunger retraction to release to the obturator nutating to  $\theta^*$ , was displayed on the timer display to the 0.0001 second. This time,  $\bar{t}^*$ , was recorded.

#### EXPERIMENTAL DETERMINATION OF THE COEFFICIENT OF SLIDING FRICTION, $\mu_s$ .

From Eq. (25) it will be noted that for large values of  $\zeta\omega_{po}\bar{t}$  the time elapsed for nutation from  $\theta_0$  to  $\theta^*$  is given by:

$$\bar{t}^* = -[(\theta_0 - \theta^*) + D]/(R\omega_{po}) + 2\zeta/\omega_{po}$$

Without the influence of fluid shear (which is negligible in this case), Eqs. (34), (35) and (39) lead to:

$$\bar{t}^* \rightarrow \pi A\omega_{po}[(\theta_0 - \theta^*) - (\lambda/2)\sin 2\theta_0]/(2\mu_s WR\sin\theta_0)$$

$$\text{as } 2\zeta/\omega_{po} \rightarrow 0$$

At relatively high spin rates, therefore, the elapsed time  $\bar{t}^*$  is expected to vary directly with  $\omega_{po}$ . Such being the case, the coefficient of sliding friction,  $\mu_s$ , may be estimated from the slope of data for  $\bar{t}^*$  vs  $\theta^*$  at high values of  $\omega_{po}$ .

#### DISCUSSION OF THE EXPERIMENTAL RESULTS

Figure 22 shows the results of experiments in which the angular velocity was varied within the range of capability of the experimental apparatus. Two balls were tested, each with different hole sizes (see Table I) but otherwise essentially identical. Also shown in Fig. 22 are the theoretical predictions given by the exact solution and by the asymptotic form of the linear approximation, Eq. (41). This latter expression has been matched to the data at high spin rates in order to obtain empirical estimates of the coefficient of sliding friction,  $\mu_s$ .

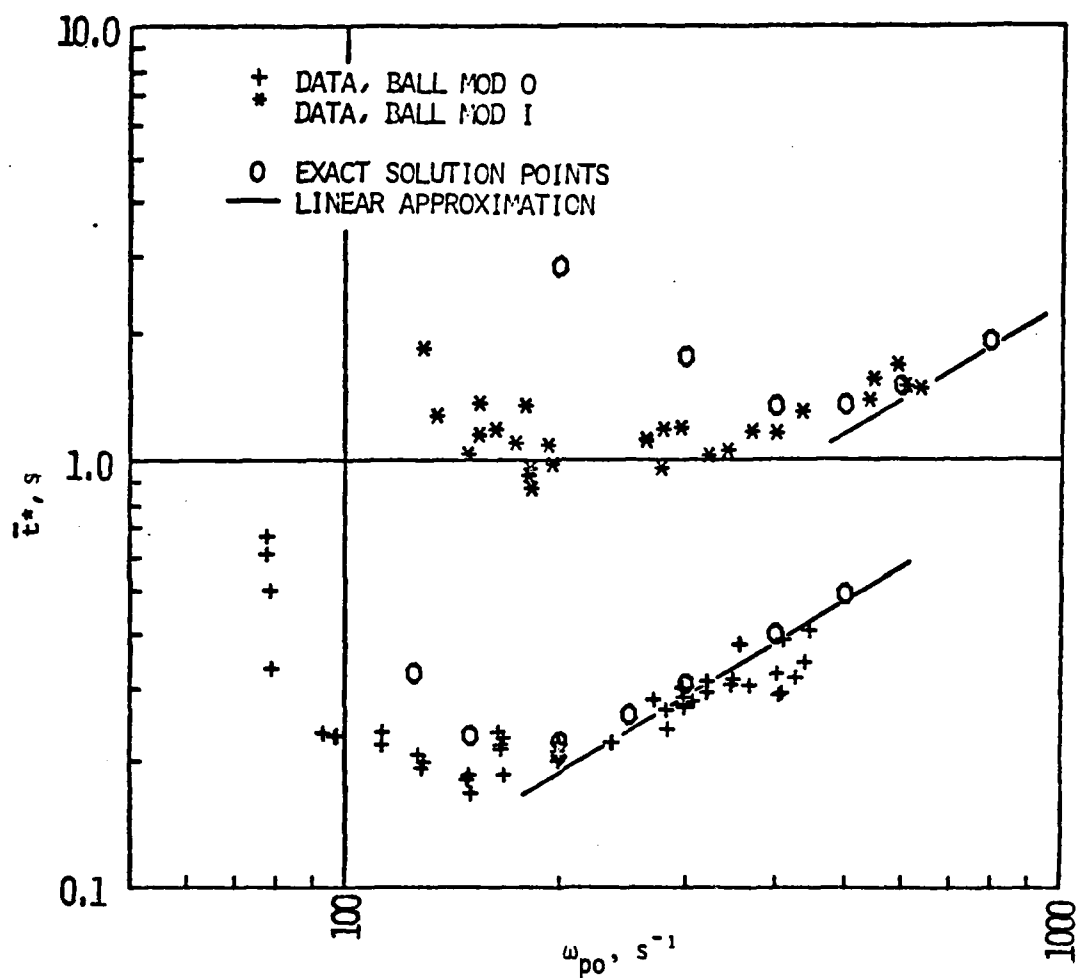


Figure 22. Presentation of experimental results showing comparisons with exact and approximate solutions. Gravity load only.

The experiments verify the theoretical prediction of the high-speed asymptote and the existence of a minimum in the elapsed time for ball-opening, with respect to projectile spin rate. The discrepancies between theory and experiment at lower spin rates (where the linear approximation is not expected to be valid) are thought to be mainly due to inadequacies in the experimental apparatus. At these low spin rates there is a prolonged period of "hover" of the ball near its initial position, followed by a rapid decrease in tilt angle (see Fig. 8). During these initial instants of time any external disturbances will tend to cause a premature conclusion of the hovering period and it is this effect that is thought to have led to the low measured values of  $\bar{t}^*$  at the lower values of  $\omega_{po}$ . The effect is more pronounced in the Mod I ball which, due to its small value of  $\lambda$ , is considerably less prone to align itself, particularly at the lower values of cavity spin rate.

The experiments were also limited in precision due to the interaction of the holding jet with the solenoid-actuated plunger. This difficulty contributed to the scatter of data and limited the maximum usable value of  $\omega_{po}$  because of the high jet pressures required to hold the ball in position at high spin rates.

The empirically determined value of the coefficient of sliding friction, 0.30 for the Mod I ball, appears to be reasonable in comparison with the value of 0.35 reported for laminated plastic on steel [15]. The larger value of  $\mu_s = 0.51$  for the Mod 0 ball is thought to be due to the influence of the relatively large hole which, in the high-speed rotating motion, will have an effect similar to that of roughness. Within the precision of the experiments there was no detectable influence of speed upon  $\mu_s$  and the assumption of a constant value for this parameter appears to have been justified, at least for the higher values of  $\omega_{po}$ .



# SENSITIVITY TESTS AND DESIGN GUIDES FOR AERODYNAMIC LOADING

Figure 11 shows a comparison of the linear approximation with the exact solution for the motion of the baseline model (Table 2) at the nominal spin rate of 115,000 RPM. Two initial ball tilt angles are also shown and it may be seen that the linear approximation yields results that are quite acceptable for initial angles near 90°. The values of M, R, and D are given on the figure for reference purposes. The usefulness and limitations of the approximate method are also illustrated in Fig. 23 where the initial opening time is given as a function of projectile spin rate. As in the experimental program this time, designated as  $t^*$ , is the time required for a straight-through path to open along the projectile centerline. The ball tilt angle at this instant is given by

$$\theta^* = \sin^{-1}(r/R)$$

and the corresponding time is a useful reference quantity for comparison of various obturator designs. (In addition, the aerodynamic force model used in this analysis becomes highly suspect at values of  $\theta$  below  $\theta^*$  since the simple shock structure assumed here will be invalid if there is any significant flow through the projectile).

Figure 23 indicates that the linear approximation approaches the exact solution at large values of  $\omega_{po}$ . This is to be expected since M decreases quadratically with  $\omega_{po}$ . The asymptotic behavior of  $\bar{t}^*$  at high  $\omega_{po}$  is a useful design insight and is given by

$$\bar{t}_{\infty}^* = A\omega_{po}[(\theta_0 - \theta^*) + D]/M\sin\theta_0$$

and for the baseline case this reduces to  $\bar{t}_{\infty}^* \approx 4.0 \times 10^{-4} \omega_{po} \text{ ms}$  ( $\omega_{po}$  in  $\text{s}^{-1}$ ). The sharp minimum in  $\bar{t}^*$  illustrated in Fig. 23 suggests some

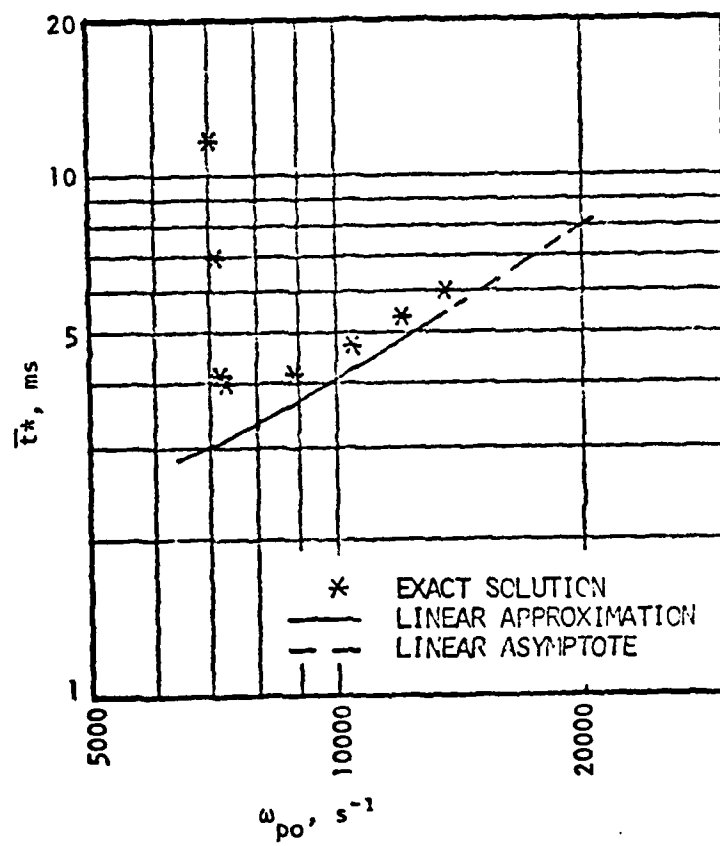


Figure 23. Comparison of approximate solutions with exact solutions.  
Baseline projectile,  $\omega_{po} = 1.20 \times 10^4 \text{ s}^{-1}$ .

caution in the design of these devices and also provides encouragement regarding the existence of criteria leading to an optimum design. The low spin-rate behavior shown in Fig. 23 is outside the linear range of operation and is due to the delaying mechanism of sliding friction at relatively large values of  $M$  (large friction, low inertial imbalance due to a small hole in the ball, and/or low projectile spin rate).

Under these conditions the ball "hovers" at its initial value and considerable time elapses before a ball orientation is achieved in which friction is in a direction to aid the alignment of the hole with the projectile axis. This behavior has been observed in previous solutions (see Fig. 8), and in the experimental program (see Fig. 22). Design guidelines necessary to avoid the hovering mode are discussed below, following a discussion of the results of the sensitivity analysis.

#### SENSITIVITY ANALYSIS

The design variables affecting the obturator performance are those contained in the normalized torque determined by Eqs. (18) - (21). The influence of the time-varying relative angular velocity and moment arms in these expressions may be qualitatively evaluated by referring to the linear approximation so that the relevant design variables are [Eq. 40]  $\lambda$ ,  $\mu_s$ ,  $F_a$ ,  $\beta$ ,  $\theta_0$ ,  $R$ , and  $\omega_{p0}$ . Since  $\lambda$  and  $\beta$  are geometric parameters depending upon the radii of the ball and its hole; and the minor moment of inertia,  $A$ , depends upon these as well as the density of the ball material, this list may also be written:  $r$ ,  $R$ ,  $\rho$ ,  $\mu_s$ ,  $M_\infty$ ,  $P_\infty$ , and  $\omega_{p0}$ . Here the aerodynamic force has been replaced by means of Eq. (21) and the projectile hole is assumed to be of the same size as that of the ball. In considering the coefficient  $\mu_s$ , it must be remembered that it depends upon the two materials (ball and projectile) and is therefore dependent upon  $\rho$ . We have studied independent variation in  $\mu_s$ , however, since its value is subject to considerable uncertainty. Experiments

have shown that the value of  $\mu_s$  should be approximately 50% larger than that published for dry friction between smooth surfaces. Table 2 indicates the baseline value for these design variables as well as the maxima and minima that determines the range of sensitivity analysis. In each case (except  $\omega_{po}$ , which has been previously discussed) the values of the variables were chosen such that equal increments were provided and the baseline condition was included in the range. Single parameter variations are shown here although work is continuing using the techniques of numerical optimization.

The computer data are presented as  $\theta$  vs  $\bar{t}$  and the interested reader may construct cross-plots such as that of Fig. 23 to evaluate the effects of these design variables upon the time required to reach a given angle, such as  $\theta^*$ . Figures 24-29 illustrate the relative importance of the selected design variables. It is important to note that in these figures the range of system performance has been restricted to the quasi-linear range previously discussed where the ball response is typically of the type shown in Fig. 8 and above the minimum in Fig. 23. Outside of this range (in the "hovering" state) the trends illustrated may be reversed. Attempts to reduce ball response time by the design improvements suggested by Figs. 24-29 may push the performance beyond the minimum illustrated in Fig. 23, with resulting "negative improvements". In many cases the implications of Figs. 24-29 are self-evident but to assist in physical interpretation a few explanatory remarks are offered below.

#### Geometry effects.

Both the ball radius,  $R$ , and the radius of the ball hole,  $r$ , were varied independently. Figure 24 shows the effects of increasing the ball radius while maintaining a constant value of  $r/R$ . The variation in this case is essentially one of scale-up which covers a range of projectile diameters from 20mm to 100mm.

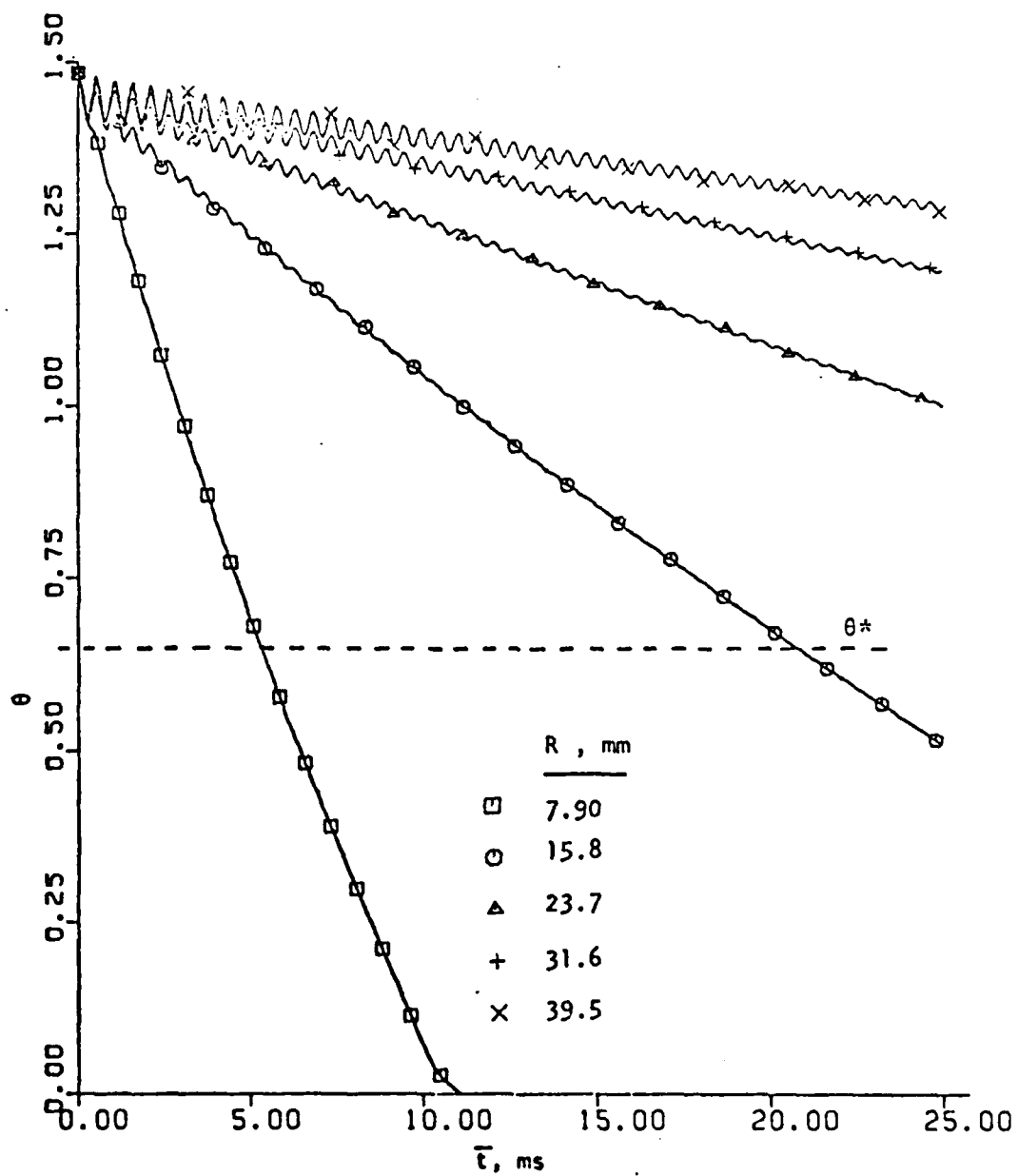


Figure 24. Effect of ball size on ball response.

It may be seen that larger systems respond more slowly. Increases in applied torques are not sufficient to offset the effects of the fifth-power relationship between ball inertia and radius. Figure 24 indicates that opening of the ball obturator in large projectiles may be unacceptably slow unless compensating design actions are taken. As will be seen in subsequent figures, such actions might include increases in ball hole radius and reduction in the density of the ball material.

Increasing the size of the hole in the ball, with all other parameters held constant, reduces the inertia of the ball and increases the imbalance between the moments of inertia about the two principal axes. Both effects are conducive to rapid ball response and this is illustrated in Fig. 25. In addition, the initial opening angle,  $\theta^*$ , is directly increased by an increase in  $r/R$  with a corresponding decrease in the elapsed time.

#### Material effects.

Though the ball-obturator must be of sufficient strength to plug the projectile during launch, it does not contribute to the structural integrity of the projectile in flight. The ball material may therefore be open to some design variation and this possibility is investigated in Fig. 26 where it is seen that the time required to reach a given ball angle is approximately proportional to the density of the ball material,  $\rho$ . A change in ball material from Carbon steel ( $\rho \sim 7,750 \text{ kg/m}^3$ ) to an Aluminum alloy ( $\rho \sim 3,100 \text{ kg/m}^3$ ) would lead to a halving of the response time. This effect also leads to an opportunity of linearly tailoring the ball response time by means of its density--a feature that may be particularly useful in applications of the system as a hydromechanical switch.

#### Coefficient of sliding friction.

As has been mentioned, the correct value of  $\mu_s$  is subject to considerable uncertainty. Figure 7 shows the impact of an uncertainty range of about  $\pm 20\%$  in  $\mu_s$  which, in terms of  $\bar{t}^*$ , is about  $\pm 15\%$ . In applications for

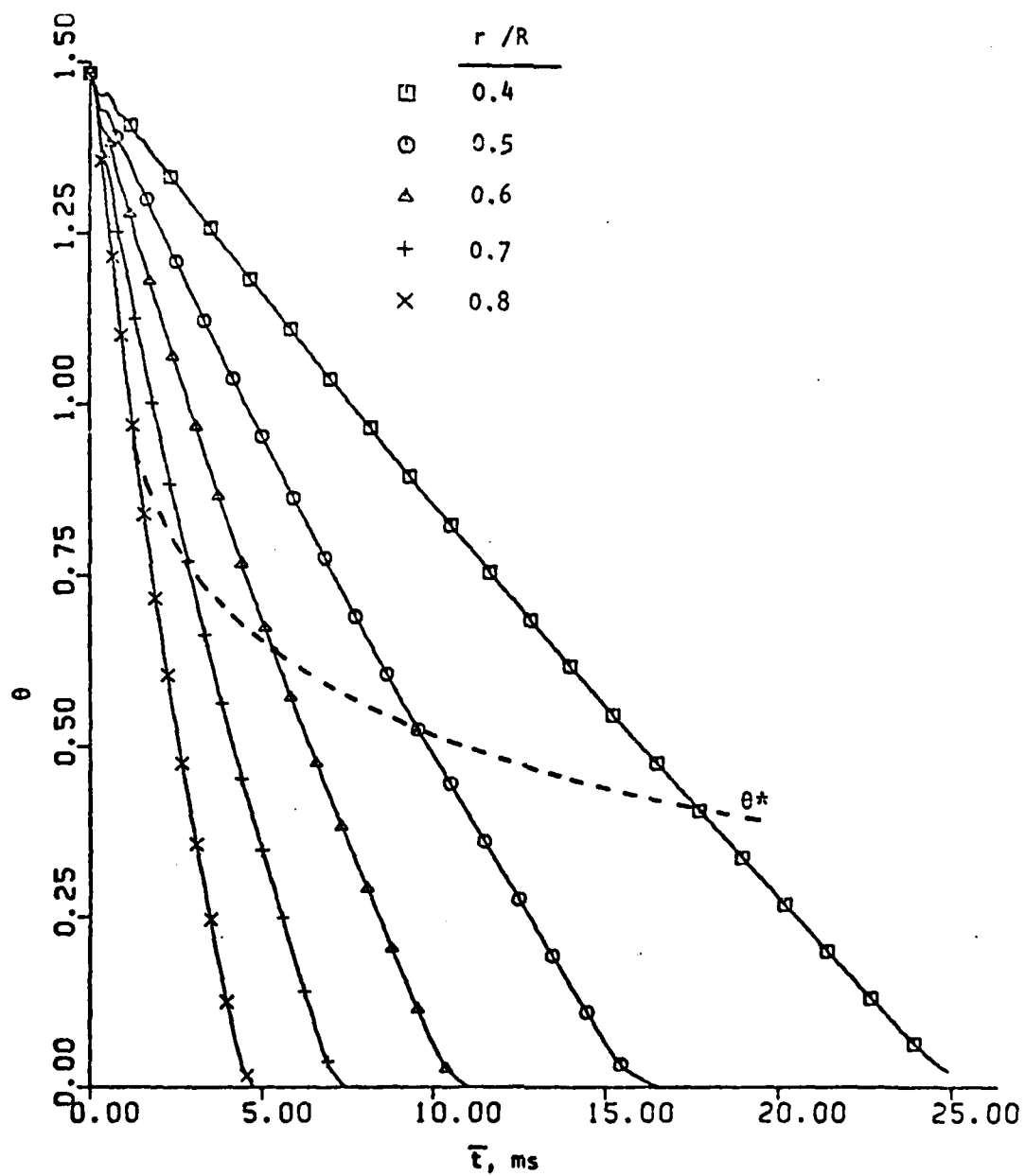


Figure 25. Effect of ball hole size on ball response.

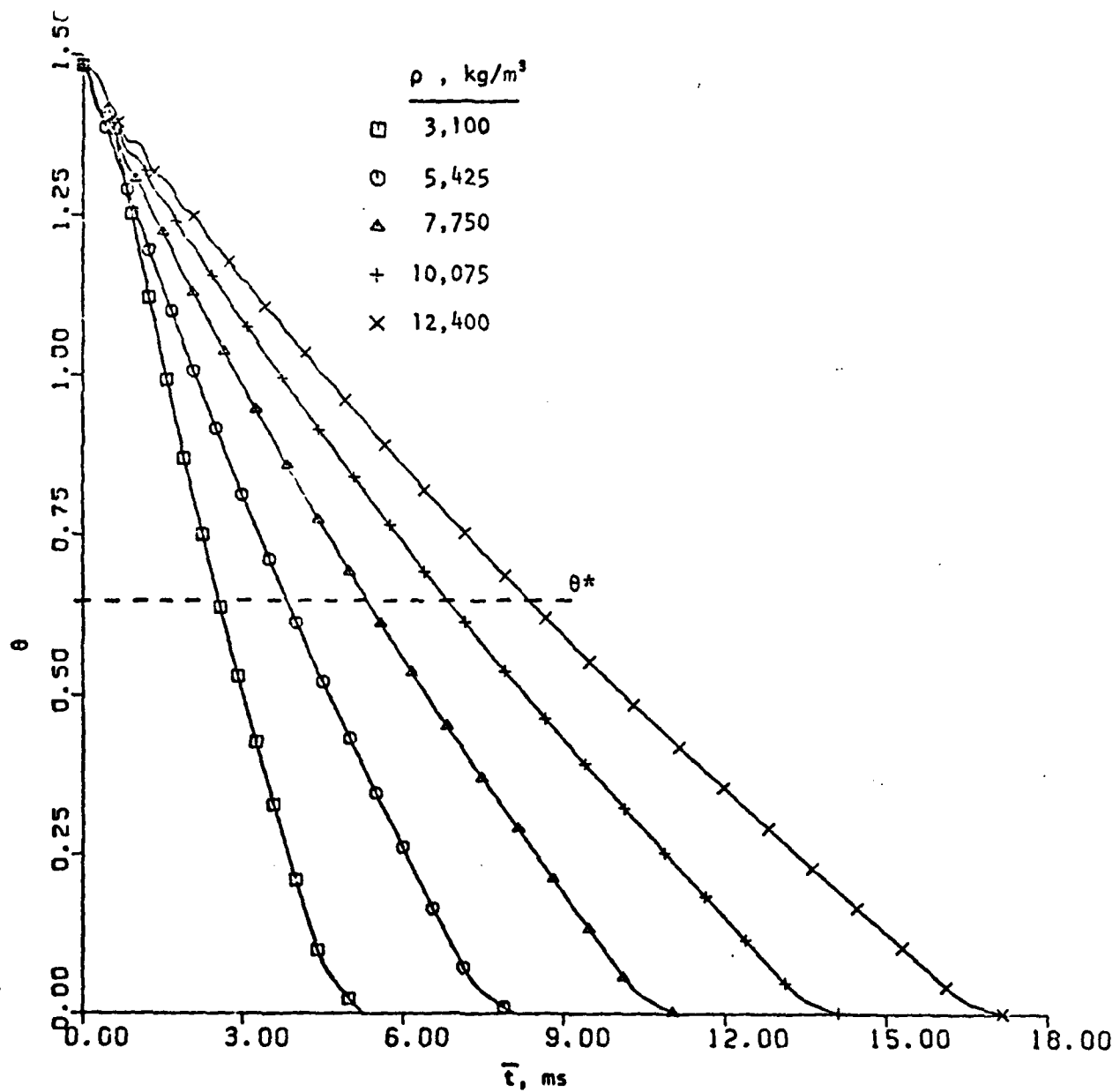


Figure 26. Effect of density of ball material on ball response.



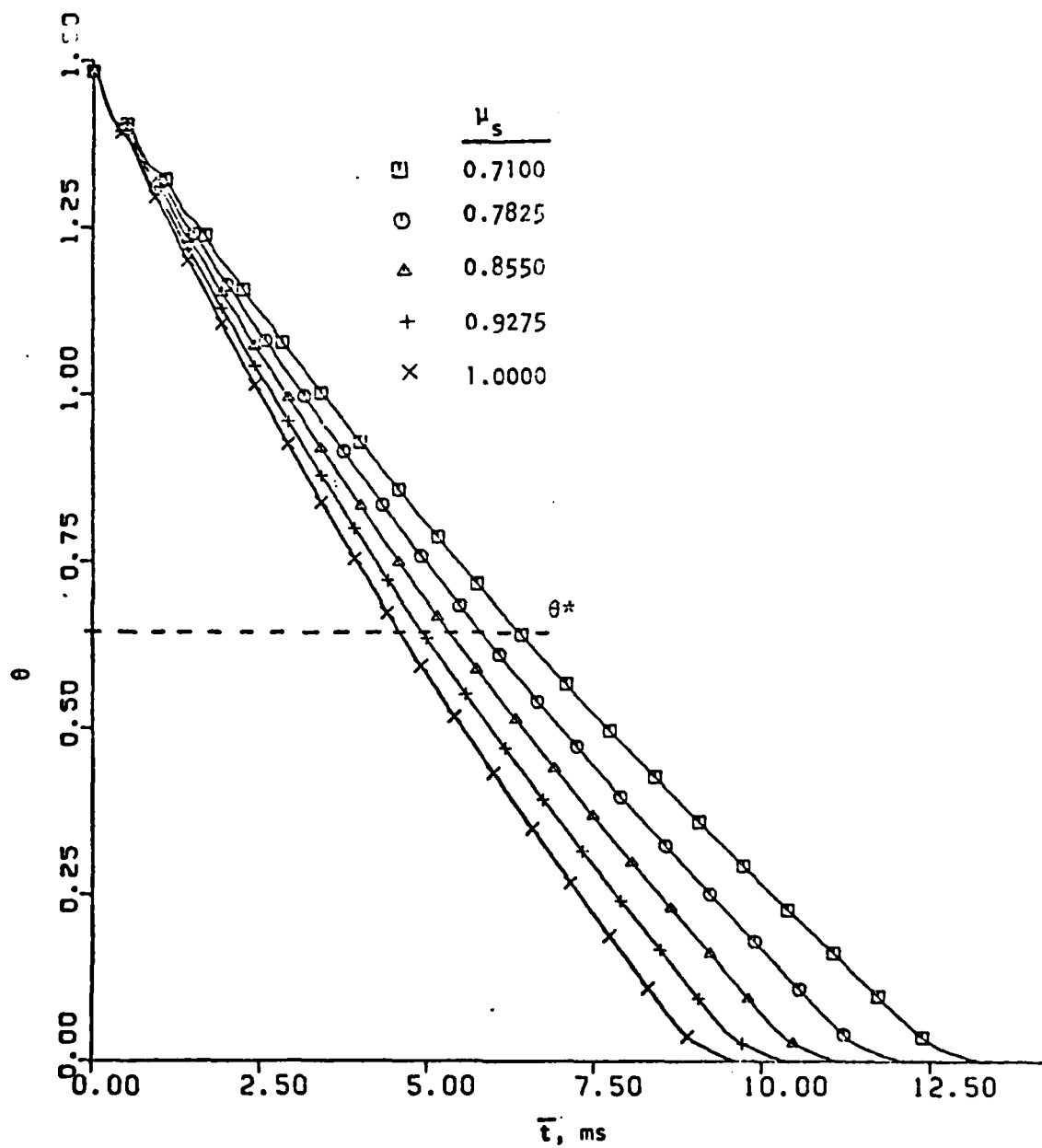


Figure 27. Effect of coefficient of sliding friction on ball response.

which margins of error such as this are unacceptable, tests of prototype configurations may be necessary to determine  $\mu_s$ . The range tested in Fig. 27 represents a best estimate for dry friction of steel on steel for the range of  $r/R$  covered in Fig. 25. Systems using dissimilar materials will require appropriate adjustments in  $\mu_s$ . In addition, it may be seen that some roughening of the interfacial surfaces may not be detrimental to system performance while, on the other hand, intentional polishing of these surfaces may lead to slower ball action.

#### Launch conditions.

Projectile launch Mach number and altitude have been separately investigated with the results shown in Figs. 28 and 29. The increase in wave drag associated with higher Mach numbers are actually beneficial in terms of ball response, because of the corresponding increases in the external moments that aid the motion of the ball within the projectile. On the other hand, increases in launch altitude lead to increases in ball response times. In proceeding from sea-level to a flight-level pressure of 0.325 atm (about 30,000 ft in the standard atmosphere), for example, a threefold increase in  $\bar{t}^*$  is predicted for the baseline design.

#### DESIGN GUIDES

The linear approximation previously developed represents a significant simplification to the computational tasks required for the exact solutions. As such, this simplified approach is recommended for design and "first-cut" calculations. As has been seen, however, there is a minimum in elapsed time (see Fig. 23, for example) which represents a demarkation of the limit of validity of the linear approximation as well as a point of optimum design for the ball obturator. A means for estimating this optimal point is developed below.

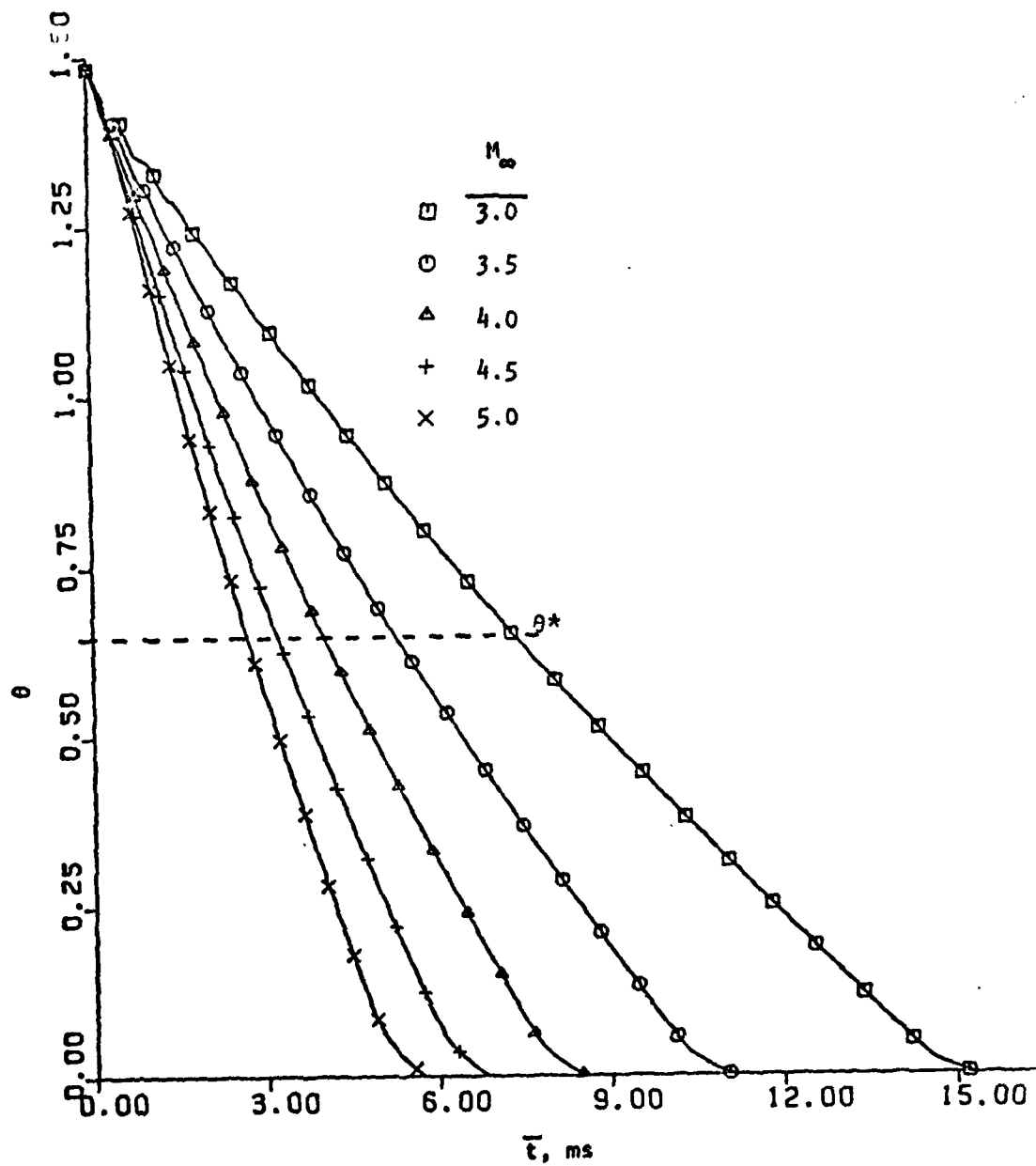


Figure 28. Effect of launch Mach number on ball response.

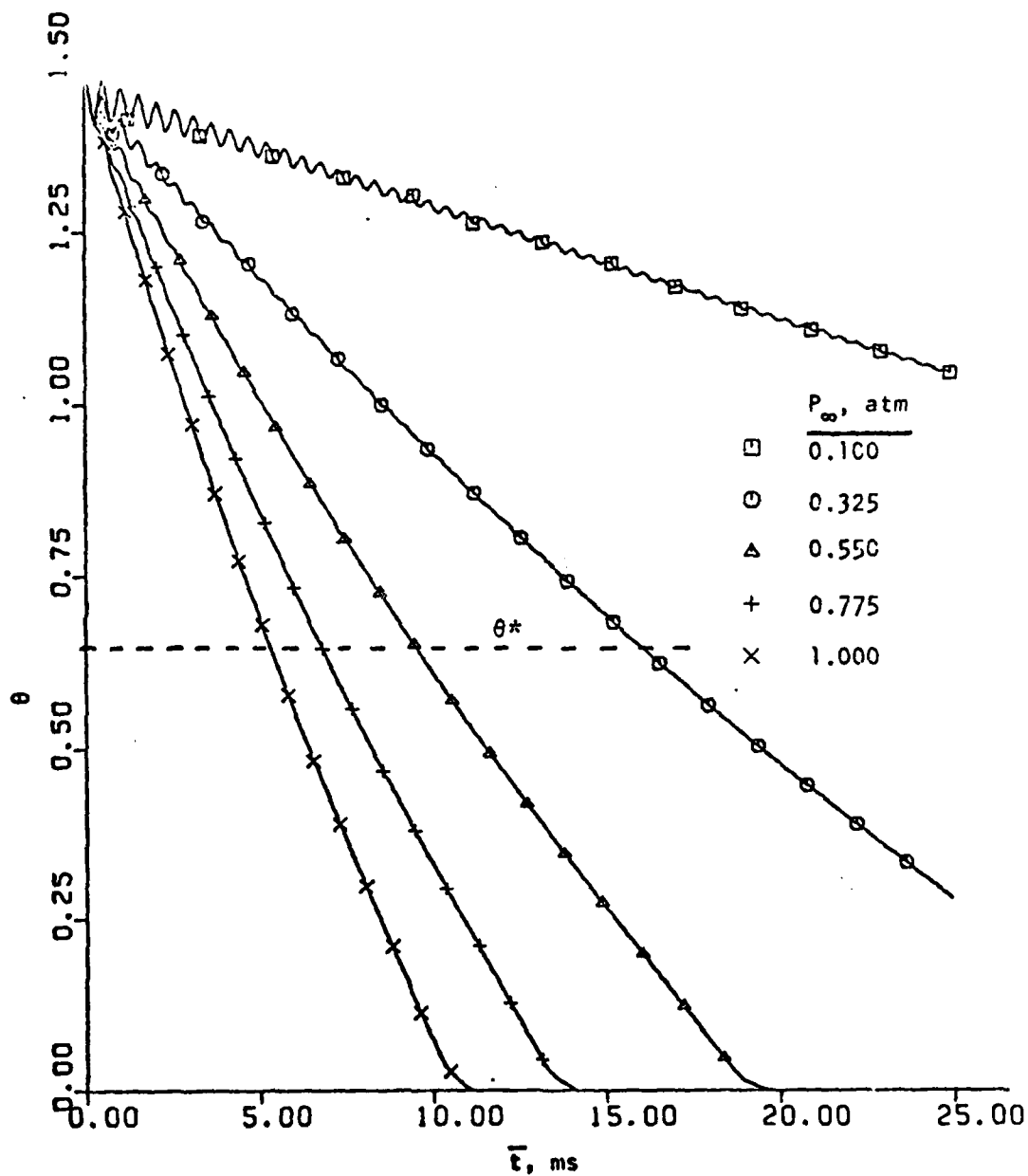


Figure 29. Effect of launch level pressure on ball response.

Under the initial conditions of the problem at hand ( $\dot{\psi}=1$ ,  $\dot{\phi}=0$ ,  $\dot{\theta}=0$ ,  $\theta=\theta_0$ ) the equations of motion [Eqs. (8) - (10)] may be written:

$$\ddot{\psi} = \dot{\theta}_0 \cot \theta_0$$

$$\ddot{\phi} = -\dot{\theta}_0 \cos 2\theta_0 / \sin \theta_0$$

$$\ddot{\theta} = -M\dot{\theta}_0 - (\lambda/2)\sin 2\theta_0$$

Here the term  $M\dot{\theta}_0$  is retained since it may be significant for large values of  $M$  even though  $\dot{\theta}_0$  is initially zero. In addition, in the initial instants of motion, the relative motion of the two bodies is largely due to nutation. That is,  $\omega_r \approx -\dot{\theta}_0$ , and

$$M\dot{\theta}_0 \approx -\bar{M}/A\omega_{po}^2$$

Thus an approximation to the initial acceleration  $\ddot{\theta}$  is given by

$$\ddot{\theta} \approx (\bar{M}/A\omega_{po}^2) + D = \text{constant}$$

In cases in which hovering occurs this expression will be approximately zero and an indication of a hovering design is therefore given by

$$\frac{\bar{M}}{A\omega_{po}^2} = -D$$

and the design guide to avoid hovering is given by

$$\frac{\bar{M}}{A\omega_{po}^2 |D|} < 1$$

In the initial instants, the applied moment due to aerodynamic loading may be conservatively estimated as  $\bar{M}_{sa} = \mu_s F_a R \cos \beta$  so that the design criterion is given as

$$H = \frac{2 \mu_s F_a R \cos \beta}{\lambda A \omega_{po}^2 \sin 2\theta_0} \lesssim 1 \quad (42)$$

where, as usual,  $\beta = \sin^{-1}(r/R)$ . Note that in this expression as  $\lambda \rightarrow 0$  or  $\theta_0 \rightarrow \pi/2$  the factor  $H$  grows beyond bound. The first situation occurs

if there is no hole in the ball ( $A = C$ ) and the second case represents the stable initial condition. Equation (42) indicates a hovering condition in both cases, in accordance with expectations.

As an example, consider the baseline case (Table II). For this design and Mach number,  $F_a \approx 93 \text{ N}$  (about 21 lb). Inserting the other constants from Table II we have

$$H = 0.735$$

and the prediction is that hovering is avoided. If the same design is considered but Eq. (42) is solved for  $\omega_{po}$  in the critical case ( $H = 1$ ) we have  $\omega_{po}(\text{critical}) \approx 10,000 \text{ s}^{-1}$  or about 98,000 rpm. Comparison of these calculations with the results indicated in Figs. 8 and 23 shows a very good agreement. In particular, Fig. 23 shows that if the equality is used in Eq. (42) a very good estimate of the optimum design is obtained. Thus, for a given worst-case launch condition (maximum  $F_a$  due to maximum Mach number and minimum altitude) and initial projectile spin rate (lowest value for worst case) the optimum ball design ( $\lambda, A, \beta, \mu_s, \theta_0$ ) may be deduced from Eq. (42). It would be wise, of course, to apply some safety factor to this optimum design and, in any case, a violation of the inequality in Eq. (42) would lead to hovering - a failure in the operation of the ball-obturator. To repeat, if the inequality is satisfied in Eq. (42) the linear approximation [Eqs. (25) and (40)] may be safely applied.

## CONCLUSIONS

The gyrodynamic motion of a ball obturator within a spinning tubular projectile has been investigated from both theoretical and experimental points of view. The theoretical developments have included both exact and approximate formulations and comparison of these two theories has led to the definition of the range of validity of the approximate method.

The experimental program was conducted under conditions in which the main source of external moment was sliding friction due to the weight of the ball. The results of these tests have substantiated the validity of both the exact and approximate theories and have led to several insights regarding the motion. In addition, a semi-empirical method of measuring the coefficient of sliding friction evolved from the experimental program.

Two distinct regions of motion have been identified. The first of these - the hovering mode - is characterized by a metastable initial orientation for prolonged periods of time. This undesirable behavior may be avoided if design guides developed within this study are followed.

The second region of motion occurs when the hovering region is avoided and in this mode, the response of the ball is approximately linear. The analysis has shown that minimum ball-opening times may be expected for ball designs and projectile launch conditions that are near (but not beyond) the onset of hovering motion.

The analytical model has been used to conduct sensitivity tests to determine the relative influence of design parameters for ball designs that are in the proper (non-hovering) range. In general, ball response is more rapid for larger hole sizes, lighter material, greater sliding friction, higher launch Mach number, and lower launch altitudes. Small obturating balls will respond more quickly than large ones, all else being equal. The theoretical

predictions depend directly upon the nature and magnitude of the aerodynamic load acting upon the ball in flight. Uncertainties regarding the theoretical description of this load are the main source of doubt regarding the precision of the predictive models presented herein.



### LIST OF REFERENCES

1. Whitworth, Joseph, Miscellaneous Papers on Mechanical Subjects, J. and J. Thomson, 1858.
2. Ballistics Research Laboratory Report 460, Retardation of Tubular Projectiles Developed From 20- mm American Ball, by A. C. Charters and R. N. Thomas, Apr. 1944.
3. Army Ballistics Research Laboratory Technical Report 02100, On the Overall Ballistic Performance of Tubular and Non-tubular Kinetic Energy Projectiles, by Frank and McLaughlin, Sept. 1978.
4. Air Force Armament Laboratory Technical Report 75-106, Aeroballistic Range Tests of Tubular Projectiles at Mach Nos. 1.0-3.2, by G. L. Winchenbach, et. al., August 1975.
5. Fackner, W. P., Concept Evaluation of Tubular Round for Vulcan, USARADB-195, May 1978.
6. Naval Weapons Center China Lake Technical Memorandum 4106, Vol. 4, Advanced Armor Penetrator (Tubular Projectile), by L. Smith, et.al., pp. 25-26, Dec. 1979.
7. Vehicle Research Corporation Report No. 26, High Performance Hollow Projectiles, by Scott Rhethorst, et. al., Aug. 1973.
8. Air Force Armament Test Laboratory Technical Report 77-109, Spinning Tubular Projectile Test Program, by T. D. Kitchun and J. W. Keeser, Jr., September 1977.
9. Brunsvold, R. S. and Kalivretenos, C. A., "Spinning Tubular Projectile", Proceedings of the 10th Navy Symposium on Aeroballistics, v. 4, pp. 52-82, July 1975.
10. Bloomer, J. W. II, "Ball Oburation of a Spin-Stabilized Tubular Projectile," Mechanical Engineer Thesis, Naval Postgraduate School, Monterey, June 1980.
11. Vehicle Research Corporation Report No. 29, Analytical Study of Tubular Projectiles Employing Consumable Sabots, by Scott Rhethorst, et, al., October 1975 (Revised April 1975).
12. Thomson, W. T., Introduction to Space Dynamics, John Wiley & Sons, N.Y. 1961.
13. Nakabayashi, K., "Frictional Moment of Flow Between Two Concentric Spheres," One of Which Rotates, J. of Fluids Engineering, Transactions of ASME, Vol. 100, No. 1, pp. 97-106, Mar. 1978.

14. Shultz, D., and Greenspan, D., "Improved Solution of Steady, Viscous, Incompressible Flow Between Two Rotating Spheres," Computers and Fluids, Vol. 7, 1979, pp. 157-163.
15. Baumeister, T. and Marks, L. S., Standard Handbook for Mechanical Engineers, 7th ed., p. 3-35, McGraw-Hill, 1967.

### LIST OF SYMBOLS

A	Mass moment of inertia about minor axis
C	Mass moment of inertia about major axis (axis of hole in ball)
D	Step input associated with linear model
$\underline{e}$	Unit vector
F	Force
h	Gap width separating ball and cavity (fluid friction model)
H	Design criterion, see Eq. (42)
k	Ratio of specific heats
M	External moment (also used to denote Mach number)
P	Pressure
r	Radius of hole in ball
R	Radius of ball
R	Slope of ramp input associated with linear model
$r_m$	Moment arm
t	Time

### Greek Letters

$\beta$	Angle used in locating contact points ( $= \theta^* = \sin^{-1}r/R$ )
$\gamma$	Angle used in locating contact points (see Fig. 5)
$\epsilon$	Dimensionless gap width ( $= h/R$ )
$\zeta$	Damping coefficient associated with linear model
$\eta$	Angle used in locating contact points (see Fig. 5)
$\lambda$	$(C - A)/A$
$\mu$	Molecular viscosity of fluid in gap
$\rho$	Density of ball material

## LIST OF SYMBOLS

### Greek Letters (continued)

- $\phi$  Phase angle associated with linear approximation (see Eq. 25)  
 $\phi, \psi, \theta$  Euler angles  
 $\omega$  Angular velocity  
 $\omega_p$  Spin rate of projectile

### Subscripts

- 1,2,3 Refer to body fixed axes  
a Aerodynamic quantity  
f Fluid quantity  
g Refers to gravity load  
n Normal component  
o Initial quantity (also refers to solutions of torque-free motion)  
r Denotes relative angular velocity  
s Associated with sliding friction  
x,y,z Refer to inertial (projectile-fixed) axes  
 $\sim$  Vector quantity  
 $\infty$  Conditions in free stream

### Superscripts

- Dimensional quantity - absence infers non-dimensionalized time-dependent quantity. E.g.  $\dot{\theta} = \dot{\theta}(\omega_{po})$ .  
\* Refers to condition of first opening of line-of-sight along projectile axis and through hole in ball obturator

DISTRIBUTION

Director Defense Documentation Center 5010 Duke Street Alexandria, VA 22314	2
Department of Mechanical Engineering Code 69 Naval Postgraduate School Monterey, CA 93940	1
Library Naval Postgraduate School Monterey, CA 93940	2
Dean of Research Naval Postgraduate School Monterey, CA 93940	2
Prof. Robert H. Nunn Code 69Nn Naval Postgraduate School Monterey, CA 93940	10
Commander Naval Weapons Center China Lake, CA 93555 Code 3205 (L. H. Smith) Code 3247 (J. S. Ward)	5 2
LT J. W. Bloomer II 7601 Hardy St. Overland Park, KS 66204	1
Dr. William Oberkamp Div. 5631 Sandia Labs Albuquerque, NM 87185	1
Dr. R. S. Brunsvold Code K82 Naval Surface Weapons Center White Oak Laboratory Silver Spring, MD 20910	1
Mr. Miles Miller Edgewood Arsenal Aberdeen Proving Ground Aberdeen, MD 21001	1

**IN  
DATE  
ILME**